Date paper written: January 10, 2016

YIELDING OF ROCKFILL IN RELATIVE HUMIDITY CONTROLLED TRIAXIAL EXPERIMENTS

Eduardo E. Alonso	Professor of Geotechnical Engineering. Department of Geotechnical Engineering and Geosciences. Universitat Politècnica de Catalunya, Barcelona, Spain.
Enrique E. Romero	Director of Research. Department of Geotechnical Engineering and Geosciences. Universitat Politècnica de Catalunya, Barcelona, Spain.
Enrique Ortega	PhD. Department of Geotechnical Engineering and Geosciences. Universitat Politècnica de Catalunya, Barcelona, Spain.

Corresponding author: E. E. Alonso
Department of Geotechnical Engineering and Geosciences.
Edificio D-2. Campus Nord. UPC. 08034 Barcelona
Phone: 34 93 401 6866; 34 93 401 7256
Fax: 34 93 401 7251
e-mail: eduardo.alonso@upc.edu

YIELDING OF ROCKFILL IN RELATIVE HUMIDITY CONTROLLED TRIAXIAL EXPERIMENTS

Eduardo E. Alonso, Enrique E. Romero & Enrique Ortega
Department of Geotechnical Engineering & Geosciences, UPC, Barcelona, Spain

ABSTRACT

The paper reports the results of suction controlled triaxial tests performed on compacted samples of two well graded granular materials in the range of coarse sand-medium gravel particle sizes: a quartzitic slate and a hard limestone. The evolution of grain size distributions is discussed. Dilatancy rules were investigated. Dilatancy could be described in terms of stress ratio, plastic work input and average confining stress. The shape of the yield locus in a triaxial plane was established by different experimental techniques. Yielding loci in both types of lithology is well represented by approximate elliptic shapes whose major axis follows approximately the K_0 line. Relative humidity was found to affect in a significant way the evolution of grain size distribution, the deviatoric stress-strain response and the dilatancy rules.

KEYWORDS

Rockfill, gravel, plasticity, dilatancy, yield surfaces, relative humidity, triaxial tests

INTRODUCTION

Rockfill and coarse grained aggregates are commonly used in road and railway embankments, railway ballast and earth and rockfill dams. Interest on these structures is maintained throughout the world because of the availability of coarse gravelly deposits, rock quarries or excavations in rock, which are the source of granular aggregates of large grain sizes. In dam engineering rockfill shoulders provide stability to impervious cores. Also, concrete face rockfill dams (CFRD) are a preferred design when impervious materials are scarce. A critical aspect of the design of CFRD is to ensure a small deformability of the embankment in order to avoid the risk of face cracking. The construction of rockfill embankments for high speed train lines raises also the need for a precise prediction of expected deformations.

Rockfill behaviour was investigated in the past century by authors involved in the design of earth and rockfill dams, especially in the US and Mexico (Fumagalli, 1969;

Marachi et al., 1969; Marsal, 1973). A few large scale experimental programs performed in the 70s provided a good basic understanding of the behaviour of reduced scale rockfill. Essentially, the tested specimens were fairly uniform gravels. Tests were conducted with the purpose of obtaining two fundamental characteristics: strength and compressibility.

Some experimental findings pointed out significant differences between rockfill and soils. It was realized, for instance, that strength envelopes had a significant curvature especially for the small stress range. De Mello (1977) in his Rankine lecture about embankment dams suggested a power function,

$$\tau_f = A(\sigma / p_{atm})^b \qquad (1)$$

to describe the shear strength of rockfill (normal stress is normalized with respect to atmospheric pressure, p_{atm}, to avoid problems with units). This equation, where A and b ($b < 1$) are constants, was used by Charles & Watts (1980) and Charles & Soares (1984) to examine the effect of a nonlinear strength envelope on the stability of rockfill slopes.

It was also observed, in oedometer tests performed in the 60s and 70s (Sowers et al., 1965; Fumagalli, 1969; Rzadkowsky & Zurech, 1970; Nobari & Duncan, 1972; Marsal, 1973; Clements, 1981) that wetting the rockfill specimen under a sustained load led to a sudden settlement (collapse). This "stress path" is to be expected "in situ" during the impoundment of the reservoir. Compressibility increased also for a wet material if compared with a dry one. These observations were explained by the breakage of particles during testing. Marsal (1973) and Hardin (1985) proposed indices to quantify the amount of particle breakage.

Wetting tests performed during triaxial testing (Veiga Pinto, 1983; Naylor et al. 1986) also resulted in a transient collapse of the specimen, in a sudden reduction of deviatoric stress and in a permanent reduction of the shear strength. Similar results were already reported by Nobari & Duncan (1972) who tested crushed claystone from Pyramid dam. Particle breakage was generally attributed to the loss of strength of particles because of water action.

Oldecop & Alonso (2001) explained relevant aspects of macroscopic rockfill behaviour and, in particular, the effect of water, from the perspective offered by fracture mechanics concepts applied to the phenomenon of crack propagation in individual particles. They reported the results of oedometer tests of compacted slate gravel under relative humidity (RH) controlled conditions. It was found that there was no need to

flood a sample to get a collapse of the granular arrangement. In fact *RH* controlled in a continuous manner the development of collapse deformations. A strain hardening elastoplastic model was then proposed to characterize the macroscopic compressibility observed in tests. Later Chávez & Alonso (2003) and Chávez (2004) presented the results of RH control triaxial tests on the same compacted slate gravel tested previously under oedometer conditions. The fundamental role of *RH* was again demonstrated. Some apparent testing inconsistencies (the decrease of initial modulus with increasing confining stress) were explained by particle breakage phenomena. This behaviour was already clear in high stress testing of sands (Yamamuro & Lade, 1996). A more advanced strain and work hardening elastoplastic model was also proposed by Chávez & Alonso (2003) on the basis of the available information.

Interest in rockfill mechanics has received considerable attention in recent years. The results of testing programs involving relatively large cells and the development of elastoplastic constitutive equations which include specific features to represent particle breakage have been reported by a number of authors (Yasuda and Matsumoto, 1994; Yasuda et al.,1997; Daouadji et al, 2001; Varadarajan et al., 2003; Indraratna et al., 1993, 1998, 2005; Lackenby et al., 2007; Indraratna & Salim, 2005; Einav, 2007a,b; Indraratna et al., 2010; Xiao et al., 2014a,b).

However, the effect of *RH* on rockfill behaviour has been largely ignored both in experiments and in constitutive modelling despite its fundamental effect. The behaviour of rockfill dams under reservoir impoundment or climatic conditions, illustrated in detail in the analysis of real cases (Alonso et al., 2005, 2011), points out the significance of water action for a wide class of rockfill materials.

Particle breakage depends on a few variables: strength (or toughness) of particles, grain size distribution (GSD), grain geometry and degree of weathering, stress level, and relative humidity. Of particular importance are the scale effects, which may be explained if one considers the size effects present in the failure of brittle materials: the rock grains themselves. Scale effects make it difficult to extrapolate test results obtained at a reduced scale to prototype conditions. Scale effects have been discussed in Alonso & Montobbio, 2002; Ramon et al., 2008; Frossard et al., 2012 and Ovalle et al., 2013.

This paper presents experimental observation on yielding states and plastic flow of compacted samples of two gravelly aggregates (Pancrudo slate gravel and limestone ballast) tested under triaxial conditions. Pancrudo gravel comes from the stabilizing shoulders of Lechago dam, an earth and rockfill dam described and analyzed in Alonso

et al. (2011). The maximum grain size "in situ" was 9 cm. The grain size distribution of the tested material had a maximum size of 5cm but otherwise was very similar to the dam material. The parent rock was Cambric quarzitic slate, highly fractured. Particle shape (Fig. 1a) was elongated and planar. This shape is expected to favour particle splitting during testing. Index properties are given in Table 1. The slate has a medium unconfined strength (20 MPa on average) and it has a relatively porous matrix (n = 8% on average). *RH* effects on compressibility and time dependent behaviour of Pancrudo gravel has been reported in Oldecop & Alonso (2001, 2003). Some information on the triaxial behaviour of this granular aggregate was given by Chávez & Alonso (2003).

There was an interest in testing gravel of a markedly different material: a sound, low porosity and strong limestone typically employed in railway ballast (Fig. 1b and Table 1). Since the effect of *RH* (or total suction) was one of the objectives of the research, it was thought that a significant change in porosity could help to understand the effect of water energy on the overall behaviour of the aggregate. A connected, relatively high porosity of the rock matrix, may lead to interpretations in terms of capillary effects and local moisture transfer on particle behaviour. In a very low porosity rock voids are probably not connected and capillarity and local water transfer are not expected to be relevant at least at the time scale of experiments. The crushed limestone had a maximum particle size similar to the Pancrudo slate but the particles had pyramidal geometries and no dominant dimensions. Particle splitting during loading was less likely in this aggregate.

A comparison between the yielding and plastic flow properties of these two widely different gravelly material helps to understand the role of rock matrix properties and particle shape on macroscopic behaviour. Data on the evolution of grain size distribution during loading will also be given. Relevant questions for constitutive modelling such as the existence of critical states, the shape of yielding loci and the dilatancy rules will also be discussed in the paper for the two tested materials.

SUCTION CONTROLLED TRIAXIAL TESTS

Water retention and grain size

The limestone rock comes from a quarry a few kilometres south from Barcelona (Garraf mountain range). It is first extracted by blasting and then crushed to the desired size.

The maximum particle size in the tests performed was 40mm. The gravels exhibit a high superficial roughness, angular sharp corners and regular sizes (Fig. 1b).

The water retention curves (WRC) for the limestone rock are given in Figure 2. Two techniques were used to determine the curve in Figure 2. For low suction values (less than 2.5 MPa) a ceramic suction plate was used. Samples are placed in contact with a saturated ceramic disk (maintained at zero water pressure) whose air entry value is larger than 2.5 MPa. Suction is induced by increasing air pressure on the rock sample (a technique known as axis translation). Higher suctions, up to 400 MPa, were imposed by a controlled atmosphere which was circulated around the rock sample until equilibrium was reached. The rock is essentially dry at such a high suction.

The WRC curve for the slate is plotted in the same figure. Three different testing techniques were used in this case: negative water column for very small suction values, an axis translation (air overpressure) for intermediate suction values and vapour equilibrium technique for high suctions. Details of these techniques are given in Tarantino et al (2009). The porous slate stores significantly more water than the limestone. No definite air entry value could be defined for the slate.

If one considers the gravel sample as a porous material, very small suction values, as low as a few kPa, are capable of removing the inter particle water from an initially saturated sample. Beyond this suction all the remaining water is stored inside the particles and the gravel looks like a dry material.

The grain size distribution of the limestone gravel used in this investigation is shown in Figure 3a. The gravelly soil is a well graded mixture with particles sizes covering the range 40–2 mm. Letter "*W*" refers to this soil. *W* samples were compacted into a metallic mould lined by a rubber membrane to the energy of the Standard Proctor test. A void ratio $e_0 = 0.504 \pm 0.02$ was achieved. Samples for triaxial testing had 250 mm in diameter by 500 mm in height in all tests performed. The compaction energy necessary to create the initial void ratio results in grain crushing which is quantified by the variation in the grain size distribution (Figure 3a)

The initial grain size distributions of Pancrudo slate and *W* samples of limestone were essentially identical. They are given in Figure 3b. Changes in grain size distribution after compaction were also very similar for the two materials (almost no difference when represented in the same plot). Compaction lead to a measurable increase in fines, better detected in a logarithmic scale of particle diameter.

Triaxial tests

Triaxial tests were performed in a *RH* controlled triaxial cell described in Chávez (2004) and Chávez et al (2009). *RH* inside the specimen was maintained by a flow of moist air. *RH* was measured by means of a capacitive hygrometer located in the moist air circuit in a point close to the specimen. Volume change was measured by two alternative procedures: the liquid level inside a double walled enclosure of the sample and by means of three measuring rings placed around the specimen. Water level inside the double walled chamber was measured by means of differential pressure transducer which reads pressure differences inside and outside the chamber. Local radial strain measurements at three levels along sample height were interpolated in order to calculate volume changes. Vertical deformations and vertical loading were also measured inside the cells. Figure 4 shows three instants of the process of sample installation inside the double walled cell.

Gravel specimens were directly compacted against the cell base by means of a split mould internally lined with a 4 mm thick neoprene membrane.

The well graded limestone material (*W*) was compacted in six layers. A Marshall hammer was used to apply 124 blows per layer. Compaction energy was close to 650 joule/litre, a value similar to the nominal compaction energy of the Standard Proctor test. Once compacted, the split mould was removed and a small confinement was applied to maintain the specimen geometry. The tamping compaction method induced some particle breakage which was illustrated in Figure 3. The calculated Marsal & Hardin indices (B_g = 10.14 and B_r = 0.11) show a moderate breakage of particles. The uniformity coefficient changed from 2.9 before compaction to 3.4 after compaction.

Relative humidity in the circulating air flow from the bottom to the top of the specimen was imposed by a saline solution. When thermodynamic equilibrium is reached inside the specimen, the psychometric law allows the calculation of the equivalent total suction which is the value reported later in plots.

Triaxial test results on *W* samples of limestone gravel could be compared with suction controlled triaxial tests on well graded specimens of Pancrudo slate since the initial void ratio of both materials (e_0 = 0.544 for the limestone gravel and e_0 = 0.59 for the slate gravel) as well as the grain size distributions were similar.

The stress paths imposed on limestone gravels are described in Figure 5. In a basic series of tests, specimens were confined isotropically at three *RH* values (10%, 50% and 100%) and sheared in compression at constant *RH*. These tests provided information on

stress-strain behaviour and dilatancy. Three confining stresses were selected: 0.3, 0.5 and 1MPa. Only the stress paths for σ_3 = 0.3 MPa and σ_3 = 1 MPa are shown in Figure 5 for clarity. Path AB shows the deviatoric loading at a suction of 250 MPa (*RH* = 10%). In some tests performed at RH=10% the specimen was flooded at an advanced state of shearing but straining was not interrupted. The sample reaction is a contraction (collapse) and the applied shearing load decreases suddenly. This is shown by the path BC in Figure 5. Suction decreases to zero and the deviatoric stress reaches some deviatoric stress (Point C) which is the result of the transient loss of sample stiffness and the rate of strain application by the loading plates. Eventually, the sample reacts to continuing straining (Path CD) by increasing the deviatoric resistance and reaches a limiting condition for saturated conditions (Point D). Note that the exact location of point C does not depend only on the mechanical constitutive behaviour: Other testing details such as the rate of change of suction at the specimen boundary compared with the rate of vertical strain, the specimen permeability and its water retention properties will control the position of C (from a modelling point of view). In a variant of this path, the specimen was effectively unloaded at C (q = 0) and then reloaded along a compression path.

Triaxial tests on slate gravel followed essentially the same stress paths although confining stresses and suction values were not the same in all samples tested. In tests on slate gravel, suction was maintained constant throughout the tests.

Specific tests to investigate the shape of the yield surface in the (p, q, s) space were also performed on slate gravel and limestone *W* specimens. They will be described later.

Test results

The results of tests performed on compacted *W* limestone gravel at three cell confining stress (σ_3=0.3, 0.5 and 1.0 MPa) and three *RH* (10%; 50% and 100%) values are collected in Figures 6a, b, c.

Specimens exhibit a ductile behaviour under all the stress and suctions tested. For a given vertical strain the mobilized deviatoric stress is systematically smaller for tests conducted at *RH* = 100%. However, the differences between *RH* = 10% and *RH* = 50% fall within the range of experimental variability. Strong positive dilatancy (contractancy) is recorded during the initial applications of deviatoric stresses; this is a consequence of particle breakage and grain contact crushing. Dilatancy rates decrease continuously as the deviatoric strains accumulate. Zero dilatancy rate is attained in the

proximity of limiting shearing conditions. Axial deformations are large at this point (8-10%). Then a second stage of negative dilatancy (expansion) is recorded, at essentially constant shearing strength.

No indication of a decrease in dilatancy rate is found at the end of tests (ε_{axial} = 16–18%). Dilatancy rate (in the negative range) increases when *RH* decreases (dryer material). The wetting episode not only implies a sudden reduction of shear stress but a distinct change in the rate of dilatancy.

For comparison, Figure 7 a,b,c shows similar tests on Pancrudo slate compacted also to a Standard Proctor energy in six layers. Now the effect of *RH* is more marked and discernible. In the six tests performed under σ_3 = 0.5 MPa for *RH* = 36%, 50%, 75%, 85%, 92% and 100% the mobilized shear stress follows a close correlation with the *RH* applied. Positive dilatancy (contractancy) now dominates the volumetric behaviour, because of the increased breakability of particles. Negative dilatancy (expansion) is again enhanced when *RH* decreases.

Ultimate void ratio states for the triaxial tests on Pancrudo slate have been plotted in Figure 8 for two *RH* values: a dry state, *RH* = 36% and a saturation state, *RH* = 100%. Critical state conditions were not reached in some of the tests but nevertheless the plot allows drawing volume-mean stress lines which seem close to a critical state condition. Void ratios are consistently higher for low *RH*. The critical state lines plotted are essentially parallel.

However a similar plot (Fig. 9) for end-of-test conditions, in the case of the limestone gravel, provides a different result. In all cases negative dilatancy rates were high at the end of the tests when vertical deformations were already very large (16–18%). No stabilized trends can be observed in Figure 9. Differences between the two represented *RH´*s (50% and 100%) cannot be identified. Tests at *RH* = 10% have not been represented because a full wetting applied before the end of the test; see Figure 6. End of test conditions exhibited a high dilation rate at the end of the tests. A linear isotropic compression line (initial state) in natural stress scale is defined by the initial states before shearing. It is concluded that critical state conditions were far from being established in the tests on hard limestone gravel.

Data presented later of the evolution of GSD and Breakage indices during testing suggest that critical state will be achieved if applied work, during testing, is capable of bringing the grain size distribution to a limiting state which could be identified by a

high fractal dimension. This is not the case of the limestone gravel (see Figure 17 and the associated discussion). In addition, the evolution of breakage indices with confining stress (Figure 16) shows that the work input into the samples, even for the highly stressed ones, is far from achieving stationary conditions. Therefore, at lower confining stresses, end of test conditions are far from achieving a limiting GSD and a zero volume change. The weaker slate planar particles (see Figures 14 and 15 for equivalent information) are closer to steady state conditions at the maximum confining stress applied but it is clear that they are also far from achieving critical state conditions.

Volumetric and deviatoric plastic strain rates were calculated during the application of deviatoric stresses (incremental elastic strains, approximated by the elastic modulus determined during unloading -see Figs. 6 and 7-, were substracted from total incremental deformations). The resulting plastic increment vectors are represented in Figure 10 for two *RH's* for the Pancrudo slate. For saturated conditions positive dilatancy (contractancy) is decreasing continuously during loading and an approximate condition of no volume change is found at the end of tests (for vertical deformations in the vicinity of 20%). Dry samples (*RH* = 38%), Figure 10b, tend to dilate moderately in two of the tests represented at the final stages of shearing but the rate of plastic volume change is already small. Defining the end of testing conditions as a critical state seems reasonable. This is further demonstrated in Figure 11 which shows the evolution of the dilatancy index (Wan & Guo, 1998):

$$D = 1 - \frac{\dot{\varepsilon}_p^p}{\dot{\varepsilon}_a^p} \qquad (2)$$

where ε_p^p and ε_a^p are the rates of plastic volumetric and axial strains, in terms of the stress ratio $R = \frac{\sigma_1}{\sigma_3}$. Critical state conditions are found for $D = 1$. The plot indicates that dilatancy paths of the four samples represented ended in a critical state. Results are similar for *RH* = 50% although the scatter of results was somewhat larger in this case.

Consider, however, a similar plot for the triaxial tests on Garraf limestone gravel in Figure 12 for *RH* = 100% and *RH* = 50%. A strong dilatancy is taking place at the end of the test, even if shear strength has already reached a stationary strength value.

The dilatancy rule for limestone gravel will be discussed further in the next section.

Strength envelopes for tests on Pancrudo slate and Garraf limestone are given in Figure 13a, b. The plot shows the non linear shape of envelope and the small effect of *RH* on

the hard Garraf limestone. Strength increases as *RH* decreases, especially in the slate gravel. Interestingly, the strength envelope for the limestone plots very close to the strength envelope for the slate tested at a high suction (*RH* = 36%).

The evolution of particle breakage was controlled in the triaxial tests performed on the slate and limestone materials. Figure 14 shows the effect of confining stress and applied suction on the accumulated grain size distribution. Also included is the effect of compaction. Both, confining stress and suction (from a very dry material, *RH* = 36% to saturated conditions) have a marked effect on breakage.

The maximum degradation is achieved for a confining stress σ_3 = 0.5MPa and saturated conditions Figure 14c. It is expected that an advanced degree of breakage leads to a self-similarity of the grain size distribution. In this case the log-log plot of the grain size distribution adopts a linear relation and the slope of this line allows the calculation of the fractal dimension of the grain size distribution. This check has been made for the triaxial test σ_3 = 0.5MPa, RH = 100%. In fact, a linear log-log plot is obtained and a fractal dimension, D = 2.16, is calculated (the slope of the log-log grain size distribution is 3-D). Similar calculations were performed for the final grain size distributions of samples tested under confining stresses of 0.1 and 0.3 MPa. Grain size distributions exhibiting the maximum breakage were selected for the calculation of *D.* The following fractal dimensions were calculated: D = 2.01 for σ_1 = 0.1 MPa and D = 2.08 for σ_1 = 0.3 MPa. The GSD distributions exhibited also a slight curvature in these two cases. Processes leading to a strong breakage of a granular material tend to show higher values of *D*. For instance, Ni et al. (2011) analyzing in situ samples of many large debris flows from Southern China found a systematic fractal dimension of grain size distributions in the range 2.6–2.75, which is higher than the values reported for triaxial tests on the slate gravel. *D* values increase with the confining stress and therefore with the amount of work input into the samples during testing.

It may be suspected that there is still some potential for particle breakage (at increased confining stress, for instance). The fractal distribution is usually regarded as an "attractor" in the evolution of grain size distribution in the process of stressing the granular soil. Also indicated in Figure 14 is the log-log plot for the initial conditions. The plot is not linear anymore and an average "fractal" number is calculated, D =1.3, which shows a significant potential for further breakage.

Hardin & Marsal indices were plotted for slate samples subjected to triaxial testing in Figure 15 in terms of confining stress and suction. The increase of breakage with confining stress at σ_3 = 0.8MPa and saturated conditions indicates that some breakage potential is still available in the samples, a result which is consistent with the fractal dimension achieved, discussed previously.

Similar results were recorded for the hard limestone. Suction and stress contributed in a significant manner to breakage. Breakage indices for similar stress – suction paths were not much different than the indices measured on Pancrudo slate. Figure 16 shows the change in grain size distribution, interpreted in terms of the breakage indices. In the case of limestone gravel the increase in breakage index due to the initial value (after compaction) is small for confining stress in the range 0.3–0.5 MPa. The influence of *RH* is also small. The confining stress dominates breakage. The comparison of the two figures suggests, however, that the breakage associated with the triaxial stress paths is lower for the limestone gravel. The evolution to fractal states is represented in Figure 17 for the highest energy applied to a limestone sample, under final saturated conditions. The final log-log plot is not straight and an average fractal dimension D = 2 is calculated. The initial grain size distribution, after compaction, is also given in the plot. An average value D = 1.5 is calculated. It appears that the limestone samples could still evolve after the triaxial testing performed. This question is probably related with the difficulty of finding critical state conditions in this case. But the straining required is probably outside reasonable values in Engineering (ballast, dams, embankments).

It was interesting to realize that breakage indices of the two materials for a similar stress path (say a triaxial test performed at a similar confining stress – 0 - 0.8 MPa – and RH) are quite similar despite the significant differences in porosity and unconfined compression strength of the slate and the limestone parent rocks. This is unexpected but results of a recent DEM modelling of coarse granular soils (Tapias et al, 2016) helps to explain the result, at least partially. It was found that changes in contact stiffness between particles did not result in a significant change in the calculated breakage index. Increasing contact stiffness leads to an increase in contact forces of the dominant internal force chains but, in parallel, the number of chain forces decreases. These two effects play an opposite role when interpreting the intensity of breakage in a granular sample.

ANALYSIS OF DILATANCY

Background

In the original Cam-Clay model (Schofield & Wroth, 1968) dilatancy was expressed as

$$d = \frac{\dot{\varepsilon}_p^p}{\dot{\varepsilon}_q^p} = M - \eta \tag{3}$$

where $\dot{\varepsilon}_p^p$, $\dot{\varepsilon}_q^p$ are the rates of volumetric and deviatoric strains ($\varepsilon_p^p = \varepsilon_1^p + 2\varepsilon_3^p$; $\varepsilon_q^p = 2/3(\varepsilon_1^p - \varepsilon_3^p)$), η is the stress ratio $\eta = q/p$; ($q = \sigma_1 - \sigma_3$, $p = 1/3(\sigma_1 + 2\sigma_3)$) and M is the stress ratio at critical state. Total stresses are considered throughout since no positive pore water pressures existed in the pores of experiments reported on gravels. For a stress ratio $\eta = 0$ (isotropic compression) Cam Clay predicts a finite dilatancy against common observations (just pure volumetric deformations which lead to $d = \infty$) Lagioia et al. (1996) proposed a modification of Equation (1):

$$d = \mu(M - \eta)(\frac{\alpha M}{\eta} + 1) \tag{4}$$

where α and μ are model parameters. Now, when $\eta \to 0$, $d \to \infty$. A few popular elastoplastic models (Modified Cam Clay –Roscoe & Burland, 1968-; Sinfonietta Classica – Nova, 1988, 1991; the single hardening models of Kim & Lade, 1988 and Lade & Kim, 1988) correspond to Equation (4) for a particular set of parameters.

Rowe (1962) in his analysis of granular materials reached the conclusion, later supported by De Josselin de Jong (1976), that d should be written as:

$$d = 1 - \left(\frac{\sigma_1}{\sigma_3}\right)\frac{1}{K_{cr}} \tag{5}$$

where $K_{cr} = \tan^2(45 + \phi_{cr}/2)$ where ϕ_{cr} is the critical state friction angle. Since $\sigma_1/\sigma_3 = (3+2\eta)/(3-\eta)$ and M and ϕ_{cr} are directly related, Equations (3), (4) and (5) relate d with the current stress ratio, η and the critical state parameter, M. In none of these models there is an explicit reference to the material density (or the confining stress).

Wan & Guo (1998) modified Equation (5) and introduced a state parameter $(e/e_{crit})^{\alpha}$ where e is the current void ratio, e_{crit} is the void ratio at critical state and α is a parameter. The proposal of Wan & Guo (1998) was followed by Chávez & Alonso (2003) and Chávez (2004) to describe the suction controlled triaxial tests on Pancrudo slate presented before. The critical void ratio was made a function of mean stress and *RH* (Fig. 8) and therefore the effect of suction is introduced into the flow rule.

Li & Dafalias (2000) discuss also the effect of density and stress level on dilatancy. From a physical perspective those two variables restrain the motion of particles during shear and therefore they should affect dilatancy. They introduced a state parameter, ψ, which is defined as the difference between the current void ratio e and the critical state value at the same confining stress, following Been & Jefferies (1985). The dilatancy rule is expressed as:

$$d = d_1\left(e^{m\psi} - \eta / M\right) \tag{6}$$

where d_1 and m are materials parameters. This formulation was also adopted by Chiu & Ng (2003) in their constitutive model for unsaturated soils recognizing that material parameters should also depend on suction. Cecconi et al. (2002) criticize also the one-to-one correspondence between d and η implied in the classic dilatancy models. They study the behaviour of pyroclastic soils, prone to particle crushing. Their experiments were interpreted in the sense that M and μ in Equation (4) evolve due to particle crushing as plastic strains accumulate.

Suction controlled testing on unsaturated soils provides also useful reference information on the effect of suction on dilatancy. Cui & Delage (1996), testing an unsaturated silt, found that in stress paths $\eta = 1$, dilatancy decreases with the increase in mean total stress and the decrease in suction. Later, Cui & Delage (1998) proposed the equation:

$$d = \mu\eta + \alpha \tag{7}$$

where α was found dependent on confining cell pressure and μ on suction in a linear manner. Equation (7), however, fails to reproduce an infinite d value for isotropic loading. Ng & Zhou (2005) testing a compacted residual soil from granite found that the maximum dilatancy depends strongly on suction and density. Suction increased the trend for negative dilatancy (volume increase). Cattoni et al. (2005) reported suction controlled tests on silty sand. They found, when plotting d against η, that the confining stress inhibited dilatancy. Suction was introduced in their analysis through a Bishop-type of effective stress.

Dilatancy of limestone gravel

If critical state conditions are not reached in triaxial experiments for a reasonably high deviatoric strain, the models outlined do not provide a suitable framework, even if some

of the ideas discussed are useful. The challenge is to analyze the dilatant behaviour of rockfill shown in Figures 6 or 12 when a critical state is not available.

Consider in Figure 18 a plot of dilatancy conditions during triaxial compression paths at RH = 50%. Plastic volumetric compressions develop during a significant proportion of the loading path. The rate of compressive plastic volumetric strains decreases continuously and this is shown by the progressive change in direction of the plastic strain increment vectors plotted. The development of dilatation plastic strains is concentrated at the limiting strength line. It appears that the normality rule is close to the actual behaviour in the final stages of specimen deformation. Similar plots were found for RH = 10% and RH = 100%. No significant effect of RH could be found in this case for the hard limestone gravel. A similar plot for the slate gravel in Figure 10 indicated that dilatancy was not so marked at the end of the triaxial loading and conditions close to critical state could be defined in a reasonable way.

A first step to establishing a dilatancy rule could be to plot d against the axial deformation. A plot of this type is given in Figure 19 for RH = 50% and RH = 10% (in the second case RH was increased to 100% when the axial deformation was high). The zero reference for the axial deformation is the beginning of the application of deviatoric stress. Compression rate is initially high but it decreases rapidly as deformation increases. Negative values are only found when the deviatoric stress is close to limiting conditions. Lower confining stresses imply higher dilatancy rates. Increasing suction contributes to increasing dilatancy, especially for low values of axial deformation.

Consider now a plot of d in terms of the normalized stress ratio η/M, where M is the value of η at a limiting state (Fig. 20). Due to the curvature of the strength envelope a varying (secant) M with mean stress has been considered (the reference M value selected for each of the triaxial tests plotted correspond to the secant M value at the limiting state for the particular test –identified as sample failure-). In some tests (for instance: “RH10%-S”), the specimen was loaded at an RH = 10% and it was saturated at vertical strains in excess of 10%, when a limiting shearing stress was already reached. In tests “RH10%-S-UR” the specimen was unloaded and reloaded once it became saturated. The confining stress dominates the plot. Dilatancy rates reach nil values when η is close to M but it becomes negative as $\eta = M$. The information at $\eta = M$ is “lumped” in a short vertical segment at the extreme of the plot. Therefore, this type of plot is not

very useful to interpret the negative dilatancy stage because dilation accumulates at an essentially constant $\eta = M$ value.

An attempt was also made to include a reference to a state parameter (the void ratio). Initial void ratio was similar in all samples tested. However, because of the small compressibility of the compacted gravel during the application of the isotropic confining stress, the void ratio of samples was controlled by the application of shearing. Void ratio first decreases and then increases as dilatancy develops. Therefore two dilatancy rates may be found for the same void ratio, which cannot be related to a critical value.

In addition to the static and kinematic constraints (confining stress, degree of packing) the breakage of particles plays a fundamental role in coarse granular aggregates. It could be quantified by the plastic work input into the specimen, W^p. Plastic work may explain particle breakage and subsequent structure rearrangements. In the dilatant regime the proximity to limiting shearing conditions dominates. Therefore dilatancy cannot be made dependent only on W^p (plastic work accumulates always in isotropic stress paths and nevertheless the dilatancy rate should be maintained at a value $d = \infty$). The proposal here is to integrate the plastic work W^p and the stress ratio η into a single coefficient ($\eta W^p/p$) which maintains the condition $d = \infty$ for $\eta = 0$ irrespective of accumulation of plastic work. The results for the series of tests performed on limestone gravel (for RH = 10% and soaking at advanced straining and RH = 50%) are shown in Figure 21a, b.

The two plots are similar and they provide a reasonable consistent interpretation of dilatancy. The effect of suction on dilatancy is small in this hard gravel. Note, however, the sudden increase in d (reduction in volume) in Figure 21a when the sample is soaked and it was already experiencing a volumetric expansion (negative d values). It is concluded that a dilatancy rule

$$d = f(\eta . \frac{W^p}{p}) \tag{8}$$

can explain the dilatancy observed in the hard limestone gravel.

The following expression:

$$d = \left(\alpha + \frac{\beta}{\left(\eta W^p \big/ p \right)^2} \right)^2 - \beta^2 \tag{9}$$

where α and β are model parameters may reproduce the measured dilatancy. A comparison of calculations using Equation (9) and measurements is given in Figure 22 for two series of triaxial tests performed at *RH* = 100% and 50% respectively. It was found: α = -4.23, β = 4.27 for *RH* = 50% and α = -3.37, β = 4.27 for *RH* = 100% . Parameters α and β depend on suction but the available data is not enough to suggest a reliable relationship.

YIELD LOCUS

The shape of the yield locus was investigated for the two reference materials.

Pancrudo slate

A procedure to determine the shape of the yielding locus is sketched in Figure 23. A position of the yield locus is first fixed at a point in the (*p*, *q*) plane. For instance, the Point A, which requires an isotropic loading. If the sample is unloaded to Point 1 and reloaded along 1-B-C it will yield at some point, which can be determined if the loading path extends somewhat beyond B (to Point C). The (curved) segment AB will be a small part of the yielding surface. If the sample is unloaded (C-2) and loaded along 2-D-E, another point of the yield surface, previously established at Point C will be identified. The procedure may continue by further unloading and reloading. Segments of a yield locus increasing in size are determined.

Identifying the shape of the yield surface requires some additional assumption. For instance, the hypothesis of accepting a suitable mathematical formulation for the (*p*, *q*) locus.

The yield locus proposed by McDowell (2000) was selected to reduce the set of yield segments into common locus:

$$\eta = q / p = M \left[(a+1) \ln \frac{p}{p_0} \right]^{\frac{1}{a+1}} \tag{10}$$

where *M* is the value of η at critical state, p_0 is the preconsolidation mean stress and a is a parameter.

Figure 24 shows in detail the stress path applied to a saturated Pancrudo slate sample (Fig. 24a) and the measured (q, ε_1) sample response (Fig. 24b). Yield points were identified in Figure 24b and transferred to the stress paths in order to define the segments of the successive yielding locus (1, 2, 3…). The numbers indicate also the loading sequence. Note that, after a first sequence of stress paths of decreasing

confining stress (1 to 10), the mean pressure was increased again and a second sequence of unloading-reloading cycles was applied (11 to 20). Equation (10) was applied to every segment identified. An approximate value $M = 1.9$ was already known for the slate gravel. Every yielding segment provides a pair (p_0, a). However, a constant average value of a was accepted and a set of p_0 values could be determined. The set of (p, q) values defining the successive yielding points were normalized by dividing them by the set of p_0 values and the resulting normalized yield curve was plotted in a common plane (q/p_0, p/p_0) (Fig. 25). The segments follow a single continuous curve characterized by a very definite "cap", which is explained by grain breakage. Also shown in the figure are the calculated incremental plastic strain vectors, a subject discussed before.

The procedure is approximate but it is capable of providing a complete shape of the yielding locus at a limited experimental effort (a single multistage test).

The identified shape of the yield curve helps to interpret tests performed under non-saturated conditions. In particular, there was an interest in checking the evolution of yielding conditions of a gravel sample, equilibrated at a given stress state under dry conditions if it is fully soaked (this is a common situation in upstream dam shells). Consider the stress paths indicated in Figure 26. A sample of compacted gravel is equilibrated at Point C following the path ABC (isotropic loading at constant suction –AB- and application of a deviatoric stress –BC-). The yield locus will pass through Point C. Three tests were performed on identical samples: all of them were initially taken to the same Point C.

- Test Uns1: Unloading (CDE) at constant suction ($RH = 36\%$; total suction: 139 MPa) and isotropic loading (EF).
- Test Sat1: Unloading and wetting (CDEG) and isotropic loading under saturated conditions (GI).
- Test Sat2: Unloading and wetting (CDEG) and deviatoric loading (Path GH).

Yield points along these paths are sketched (black dots) in Figure 26. An example of identification of the yielding point is given in Figure 27 for the stress path Sat2. The plot in Figure 27a shows the initial path to set the yielding state under $RH = 32\%$, the unloading to Point G and the subsequent deviatoric loading under saturated conditions. Figure 27b shows the sample response in (q, ε_1) plot. The drop in the yielding deviatoric

stress for saturated conditions is well identified. Note that no volumetric deformations were recorded during the unloading part of the test.

A summary of results is given in Figure 28, which shows the identified yield points for the two *RH* conditions (36%; 100%) and the expected yield loci in view of the previous findings. The dry yield locus experiences a substantial shrinkage under saturated conditions at essentially a common void ratio.

An additional aspect of interest was to check if the shape of the yield surface would experience a change when suction increases. This question was approached by conducting two series of tests on saturated and unsaturated samples initially equilibrated at the same initial mean stress-deviatoric stress state. The applied stress paths are shown in Figure 29. The initial path (OCF) has the purpose of positioning the yield surface at a common Point F (p = 0.5 MPa; q = 0.68 MPa). Then, three stress paths (three different samples) were applied by unloading to Point C, and loading to final states 1, 2 and 3. The two series of tests performed correspond to a dry state (*RH* = 42%) and a fully saturated (soaked) state (*RH* = 100%). As an illustration, the determination of the yield point for Path 2 in a saturated sample is shown in Figure 30. Figure 30a shows the stress path: unloading –FC- and deviatoric loading at constant mean stress. Figure 30b shows the determination of the yield point at q = 0.595 MPa.

The determination of the yield compression point along Path 1 for unsaturated conditions is shown in Figure 31. The stress path (Fig. 31a) shows the unloading FC and the isotropic loading. The yield point was identified at the point of change of the $\Delta\varepsilon_1$ vs. Δp slope (Fig. 31b).

Yield points are collected in Figure 32.The shape of the yield loci for saturated and unsaturated specimens are very similar. Under isotropic states yielding for saturated conditions appears to be lower than the yielding states for the dry state, but differences are small. Note that Figure 32 does not contradict the suction effects on yielding locus given in Figure 28. In fact, the saturated sample as well as the dry sample (RH = 42%) were taken to the same “F” point in the (p,q) space (Figure 29) previous to any further testing. The saturated sample experienced a significantly larger deformation (in particular, volumetric compression, which means that the saturated sample has a lower void ratio than the dry sample) than the dry sample tested at *RH* =42%. In other words, the two yield curves given in Figure 32 do not belong to the same yield surface in a (p, q, suction) space. This is not the case of Figure 28 which represents two cross sections of the yield surface at two different suctions.

Limestone gravel

Three alternative procedures were used to determine the yield envelope of the compacted limestone gravel. The results are compared in a Figure 33.

Under the first procedure, the shape of the yield locus may be approximated by a deviatoric loading test under conditions of zero volume change. In saturated soils this is achieved in undrained loading paths. In dry gravel, tested at a low shearing rate, an operator checking in real time the volume change, may control the applied confining stress in order to maintain, within certain accuracy, the condition of no volume change. The procedure would give a reasonable result for a high elastic stiffness. In fact, the elastic modulus is high for the limestone gravel: it varies between 300 and 400 MPa for confining stresses in the range 0.3–0.1 MPa. This procedure was followed in a compacted limestone gravel sample equilibrated at a RH = 50% (suction = 98MPa). The specimen was first isotropically loaded to p = 1MPa. The vertical shearing speed was fixed to 0.04mm/s. The recorded deviatoric stress during this experiment is shown in Figure 34. The (p, q) stress path is shown in Figure 33. The plotted yield curve has the shape of the narrow ellipse whose major axis rotates with respect to the p axis. K_0 conditions during compaction can be inferred from data on static compaction. A K_0 = 0.26 was measured in an instrumented large diameter oedometer cell (Oldecop & Alonso, 2004) for well graded specimens (W) compacted to Proctor energy and loaded in the normally consolidated range (Ortega, 2008). The K_0 line is also plotted in the figure. It crosses the yield locus at the point of maximum mean stress. The K_0 line is not, however, the axis of the approximate ellipse which describes the experimental shape of the yield locus.

A further approximate determination of the yield surface was performed following the procedure already described in connection with the slate gravel (Poorooshasb et al., 1967). Loading paths were interrupted as soon as yielding was identified. However, some overshoot is unavoidable. No correction for the drift of the yield curve, which is thought to be small, was applied in this case. The variation of void ratio with confining stress was plotted in real time (two examples are given in Fig. 35), the yield point was identified in real time and the loading increase was interrupted shortly afterwards. Some error accumulates, however, using this procedure, which provides only an approximation to the actual yielding conditions. The plotted loading segments in Figure 33 show the elastic paths found by the outlined procedure. Also plotted in Figure 33 is the previously determined yield locus using the zero total volumetric approach. Both

procedures are approximate but they provide a reasonable indication of the shape of the yield locus.

A third independent attempt to determine the shape of the yield curve and to investigate the flow rule at different positions on the yield locus involved testing identical specimens at RH = 50% under different stress paths. The procedure has already been described. The applied paths are shown in Figure 36. After loading samples to a confining stress of 0.6 MPa (Point A) and a deviatoric state B they were unloaded to the isotropic state A and then loaded along three alternative paths (isotropic, pure shear and compression intermediate between isotropic and σ_3 = constant). Point B was selected to be the yield point providing the deviatoric stress when the compacted specimen is isotropically consolidated to p = 1MPa. This testing protocol was also applied to a set of saturated samples compacted at the same initial density. The identified yield points are shown in Figure 33. Also indicated is the suggested shape of the yield surface on the basis of previous information.

The three series of tests provide a consistent result. The shape of the yield locus is well identified. The inner yield surfaces (for RH = 50% and 100%) correspond to a sample initially compressed to a lower stress (p = 0.6 MPa) than the other two samples tested (p = 1 MPa). The effect of RH (50 % to 100%) is small, in terms of the size of the elastic domain, in this hard limestone material

Figure 37 provides more information on the plastic flow of the compacted limestone gravel. Data for the saturated and RH = 50% cases are compared. They correspond to conditions at the end of stress paths and therefore, they are essentially at yielding states. Each one of the paths plotted ended at a relatively small vertical deformation far from steady state conditions. Volumetric expansion would develop under increasing deviatoric deformation. The differences in Figure 37 between the dry and the saturated samples are significant. The saturated sample compresses more than the dry one. Dilatancy (expansion) is only observed in the “dry” side of the yielding locus and it is more marked on the dry sample. Non-associativity is also the rule at this level of straining.

CONCLUSIONS

Two gravels having different shapes resulting from their lithology (a Cambric quarzitic slate and a hard limestone of Secondary origin respectively) were selected to investigate the yielding conditions of coarse granular aggregates and of the role of suction. Two

similar well-graded grain size distributions at the same initial void ratio were tested under several stress and suction paths. The gravel fragments in the first case are planar, elongated and exhibit sharp edges. The limestone gravel is a typical ballast material: grains have pyramidal and parallelepipedic shapes as well as sharp edges and corners. The slate has a lower strength and a higher porosity than the limestone. It may be accepted that it has also a higher grain breakage potential.

Water effects are associated with particle breakage because the velocity of crack propagation is significantly affected by water energy, which is alternatively expressed in terms of relative humidity or total suction. The slate gravel is expected to be more sensitive to water effects, if compared with the limestone gravel.

In fine granular materials (sand) of medium-high density, deviatoric loading leads, at small strains, to a contractant phase of the skeleton. In coarse materials, this phase extends to large strains due to grain breakage. Dilatancy develops after a substantial deviatoring straining. *RH* has a profound effect on dilatancy. Low *RH* values (high suction) enhance dilatancy (volumetric expansion) and reduce volumetric contractancy. This is explained by the reduced rate of crack propagation in particles in the presence of high suctions.

A consequence of the simultaneous breakage and fabric rearrangement is the difficulty to find steady state –or critical- conditions at deviatoric strains of interest in applications (say no more than 15–20%). This was especially the case of the strong limestone gravel. In the weaker slate gravel, critical state conditions could be identified. This facilitates the development of dilatancy rules and the generation of constitutive models.

A related observation concerns the evolution of grain size during testing. If a fractal distribution is accepted as an indication of a final “attractor” of the evolution of grain size, the slate material subjected to the most demanding triaxial test in terms of confining stress and water action (saturated) was closer to this final state. The limestone gravel, subjected to a similar stress suction path, exhibited a higher remaining potential for grain breakage as shown by the interpretation of the achieved grain size distribution and the rate of increase of breakage indices at the maximum confining stresses applied in the triaxial tests (0.8 – 1 MPa).

The plastic work input into the tested samples was found to be a useful quantity to interpret the dilatancy behaviour of the hard limestone gravel even if critical state conditions were not reached in tests. A dilatancy rule has been proposed. It combines, in a dimensionless parameter, plastic work, confining mean stress and stress ratio.

The geometry of yield loci of the tested compacted samples has been searched by different procedures for the two materials. They are described by irregular ellipses rotated with respect to the isotropic axis. These are shapes not different from the envelopes of fine-grained materials. A definite "cap" explains the significant yielding in compression. No significant changes in shape of the yield loci are found for variations in *RH*. Wetting from a "dry" state results in shrinkage of the current yield locus. This reduction in the elastic domain is explained by the increasing rate of particle breakage associated with wetting and the subsequent rearrangement of the structure. Tests performed at a constant rate of straining undergoing a rapid increase in RH (from "dry" to saturated conditions) react to skeleton collapse by a rapid reduction of current deviatoric stress.

REFERENCES

Alonso, E.E. & Montobbio, D. (2002) Particle size effects on rockfill compressibility. R.J. Krizek Symposium on Geotechnical Materials: Measurement and analysis. Northwestern University, Evanston, Ill. USA.

Alonso, E.E., Olivella, S. & Pinyol, N. (2005) A review of Beliche Dam. Géotechnique, 55(4): 267–285.

Alonso, E.E., Olivella, S., Soriano, A., Pinyol, N.M. & Esteban, F. (2011) Modelling Lechago earth and rockfill dam. Géotechnique, 61(5): 387–407.

Been, K. & Jefferies, M. G. (1985) A state parameter for sands. Géotechnique, 35, 2, 99-112.

Cattoni, E. Cecconi, M. & Jommi, C. (2005) Soil dilatancy and suction: some remarks on their mutual effects on the shear strength of granular soils. Proceedings of the eleventh International Conference on Computers Methods and Advances in Geomechanics. Torino, Italy, 19-26.

Cecconi, M. DeSimone, A. Tamagnini, C. & Viggiani, M. B. G. (2002) A constitutive model for granular materials with grain crushing and its application to a pyroclastic soil. International Journal for Numerical and Analytical Methods in Geomechanics, 26:1531-1560.

Charles J.A. & Watts K.S. (1980) "The influence of confining pressure on the shear strength of compacted rockfill". Géotechnique, 4 (3):353-398.

Charles, J.A. & Soares, M. M. (1984) Stability of compacted rockfill slopes. Géotechnique, 34, 1, 61 –70

Chávez, C., (2004) Estudio del Comportamiento Triaxial de Materiales Granulares de Tamaño Medio con Énfasis en la Influenciade la Succión, PhD Thesis, Universitat Politècnica de Catalunya, Spain.

Chávez, C. & Alonso, E.E. (2003) A constitutive model for granular aggregates which includes suction effects. Soils and Foundations, 43(4): 215–227.

Chávez, C., Romero, E. & Alonso, E.E. (2009). A rockfill triaxial cell with suction control. Geotechnical Testing Journal 32(3)**. DOI:** 10.1520/GTJ101590

Chiu, C. F. & Ng, C.W.W. (2003) A state-dependent elasto-plastic model for saturated and unsaturated soils. Géotechnique 53, No. 9: 809-829.

Clements, R. P. (1981) The deformation of rockfill: inter-particle behaviour, bulk properties and behaviour in dams. PhD. Thesis, Faculty of Engineering, King's College, London University.

Cui, Y.J & Delage (1996) Yielding and plastic behaviour of an unsaturated compacted silt. Géotechnique 46, No. 2: 291-311.

Cui, Y.J, & Delage, P. (1998) Plastic flow of an unsaturated compacted silt. Proceedings of de second international conference on unsaturated soils. Beijing, China, Vol.1: 467-472.

Daouadji, A., Hicher, P.Y. & Rahma, A. (2001) An elastoplastic model for granular materials taking into account grain breakage. European Journal of Mechanics-A/Solids 20 (1), 113-137

De Josselin de Jong, G. (1976) Rowe´s stress-dilatancy relation based on friction, Géotechnique 26, No.3: 527-534.

De Mello, V.F.B. (1977) "Seventh Rankine Lecture: Reflections on design decisions of practical significance to embankment dams". Géotechnique, 27(3), 279-356.

Einav, I. (2007a) Breakage mechanics. Part I: Theory. J. Mech. Phys. Solids 55, No. 6, 1274–1297.

Einav, I. (2007b) Breakage mechanics. Part II: Modelling granular materials. J. Mech. Phys. Solids 55, No. 6, 1298–1320.

Frossard, E., Hu, W., Dano, C. & Hicher, P.-Y. (2012) Rockfill shear strength evaluation: a rational method based on size effects. Géotechnique, 62(5): 415–427.

Fumagalli, E. (1969) Tests on cohesionless materials for rockfill dams. J. Soil Mech. Found. Engng Div., ASCE, 95(SM1): 313–330.

Hardin, B. O. (1985) "Crushing of Soil Particles." Journal of Geotechnical Engineering.Asce 111(10): 1177-1192.

Indraratna, I., Wijewardena, L. S. S., & Balasubramaniam, A. S.(1993) Large-Scale Triaxial Testing of Greywacke Rockfill, Géotechnique, Vol. 43, No. 1, pp. 37–51.

Indraratna, B., Ionescu, D., & Christie, H. D. (1998) Shear behavior of railway ballast based on large-scale triaxial tests. J. Geotech. Geoenviron. Eng., 124(5), 439–449.

Indraratna, B., Lackenby, J., & Christie, D. (2005) "Effect of confining pressure on the degradation of ballast under cyclic loading." Géotechnique, 55(4), 325–328.

Indraratna, B., & Salim, W. (2005) Mechanics of ballasted rail tracks. A geotechnical perspective,Taylor&Francis/Balkema, London.

Indraratna, B., Thakur, P. K., & Vinod, J. S. (2010) Experimental and numerical study of railway ballast behaviour under cyclic loading. Int. J. Geomech., 10(4), 136–144.

Kim, M.K. & Lade, P. V. (1988) Single Hardening constitutive model for frictional materials. I. Plastic potential function. Computers and Geotechnics, Vol. 5: 307-324.

Lackenby, J., Indraratna, B., McDowell, G., & Christie, D. (2007) Effect of confining pressure on ballast degradation and deformation under cyclic triaxial loading. Geotechnique, 57(6), 527–536.

Lade, P. V. & Kim, M. K. (1988) Single hardening constitutive model for frictional materials.II. Yield criterion and plastic work contours. Computers and Geotechnics, 6, 13-29.

Lagioia R., Puzrin A. M. & Potts D. M. (1996) A new versatile expression for yield and plastic potential surfaces. Computers and Geotechnics, Vol. 19, No. 3: 171-191.

Li, X. S. & Dafalias, Y. F. (2000) Dilatancy for cohesionless soils. Géotechnique 50, 4: 449-460.

Marachi, N.D., Chan, C.K., Seed, H.B. & Duncan, J.M. (1969). Strength and deformation characteristics of rockfill materials, Department of Civil Engineering, Report No. TE–69–5. University of California.

Marsal, R. J. (1973) Mechanical properties of rockfill. Embankment Dam Engineering. Casagrande Volume. Hirschfeld, R. C. & Poulos, S. J., eds., John Wiley & Sons.

McDowell, G. R. (2000) "A family of yield of loci based on micro mechanics." Soils and Foundations 40(6): 133-137.

Naylor, D. J., Maranha das Neves, E., Mattar, Jr., D. & Veiga Pinto, A. A. (1986) "Prediction of construction performance of Beliche Dam", Géotechnique 36, No. 3, 359-376.

Ng, C.W.W. & Zhou, R.Z.B. (2005) Effects of soil suction on dilatancy of an unsaturated soil. Proceedings 16 th International Conference On Soil Mechanics and Geotechnical Engineering. Osaka, Japan, Millpress, Rotterdam, Vol. 2: 559-562.

Ni, H., Zheng, W., Liu, X. & Gao, Y. (2011) Fractal-statistical analysis of grain-size distributions of debris-flow deposits and its geological implications. Landslides, 8: 253–259.

Nobari, E.S. & Duncan, J.M. (1972) Effect of reservoir filling on stresses and movements in earth and rockfill dams, Department of Civil Engineering, Report No. TE–72–1. University of California.

Nova, R. (1988) Sinfonietta classica: an exercise on classical soil modeling. Proc. Int. Symp. Constitutive Equations for Granular Non-Cohesive Soils: 501-520. Balkema-Rotterdam, Cleveland.

Nova, R. (1991), A note on sand liquefaction and soil stability. Conf. Constitutive Laws for Engineering Materials, ASME Press, Tucson, AZ.

Oldecop, L. & Alonso, E. E. (2001) A model for rockfill compressibility. Géotechnique 51, No. 2, 127-139.

Oldecop, L. & Alonso, E. E. (2003) Suction effects on rockfill compressibility. Géotechnique. 53(2): 289-292.

Oldecop, L. A. & E. E. Alonso (2004) Testing Rockfill Under Relative Humidity Control. Geotechnical Testing Journal, Vol. 27, No. 3

Ortega, E. (2008). "Comportamiento de materiales granulares gruesos. Efecto de la succión". Tesis Doctoral. Universitat Politècnica de Catalunya, Barcelona, España.

Ovalle, C., Frossard, E., Dano, C., Hu, W., Maiolino. S. & Hicher, P-.Y (2013) The effect of size on the strength of coarse rock aggregates and large rockfill samples through experimental data, Acta Mechanica, 225, 2199-2216.

Poorooshasb, H. B. Holubec, I. & Sherbourne, A. N. (1967) Yielding and flow of sand in triaxial compression: Parts II and III. Canadian Geotechnical Journal, 1967, 4(4): 376-397

Ramon, A., Alonso, E.E. & Romero, E.E. (2008) Grain size effects on rockfill constitutive behaviour. Proc. of the 1st European Conference on Unsaturated Soils. Taylor & Francis. 341–347.

Roscoe, K. H. & Burland, J. B. (1968) On the generalised stress strain behaviour of "wet"clay. Engineering plasticity: 535-609. Cambridge University Press, Cambridge.

Rowe, P. W. (1962) The stress-dilatancy relation for static equilibrium of an assembly of particles in contact. Proc. Roy. Soc. London A269: 500-527.

Rzadkowski, B. & Zurek, J. (1970) Influence de l'eau sur la déformabilité des roches broyées et sur le tassement des barrages en enrochement. Trans. 10th Conf on Large Dams, Montreal, 1, 857-867.

Schofield, A.N. & Wroth, C.P. (1968) Critical state soil mechanics. McGraw Hill. London.

Sowers, G.F., Williams, R.C. & Wallace, T.S. (1965) Compressibility of broken rock and settlement of rockfills. Proc. 6th ICSMFE. Montreal, 2: 561–565.

Tapias, M., Alonso, E. E. & Gili, J. (2016) A particle model for rockfill behavior. Géotechnique, DOI: 10.1680/jgeot.14.P.170.

Tarantino, A., Romero, E. & Cui, Y-J., eds. (2009) Laboratory and Field Testing of Unsaturated Soils. Springer. Berlin.

Varadarajan, K., Sharma, G., Venkatachalam, K. & Gupta, A. K. (2003) Testing and modeling two rockfill materials. Journal of Geotechnical and Geoenvironmental Engineering, Vol. 129, No. 3, 206-218

Veiga Pinto, A.A. (1983) Previsao do comportamento estrutural de barragens de enrocamento. PhD thesis, Laboratório Nacional de Engenharia Civil, Lisbon.

Wan R. G. & Guo P. J. (1998) A simple constitutive model for granular soil: Modified stress-dilatancy approach, Computers and Geotechnics, vol. 22, No.2: 109-133.

Xiao, Y., Liu, H., Chen, Y. & Jiang, J. (2014a) Bounding surface plasticity model incorporating the state pressure index for rockfill materials. J. Eng. Mech. ASCE, DOI: 10.1061/(ASCE) EM.1943-7889.0000802.

Xiao, Y., Liu, H., Chen, Y. & Jiang, J. (2014b) Bounding surface model for rockfill materials dependent on density and pressure under triaxial stress conditions. J. Eng. Mech., DOI: 10.1061/(ASCE)EM.1943-7889.0000702.

Yamamuro, J. A. & Lade, P. V: (1996) Drained sand behaviour in axisymmetric tests at high pressures. J. of Geotech. Engng., ASCE, 122 (2) 109-119

Yasuda, N. & Matsumoto, N. (1994) Comparisons of deformation characteristics of rockfill materials using monotonic and cyclic loading laboratory tests and in situ tests. Can. Geotech. J., 31, 162-174.

Yasuda, N., N. Matsumoto, R. Yoshioka & Takahashi, M. (1997) Undrained monotonic and cyclic strength of compacted rockfill material from triaxial and torsional simple shear tests. Can. Geotech. J., 34, 357-367.

TABLES

Table 1. Index properties of Pancrudo slate and Limestone gravel.

Property	Pancrudo slate	Limestone gravel
Uniaxial compression strength	14.2 – 31.9 MPa	67 – 146 MPa
Specific gravity	2.754	2.76
Water absortion (ASTM C97-90)	1.36%	0.38%
Porosity	6.3 – 11.8%	1%

FIGURES

Fig.1a

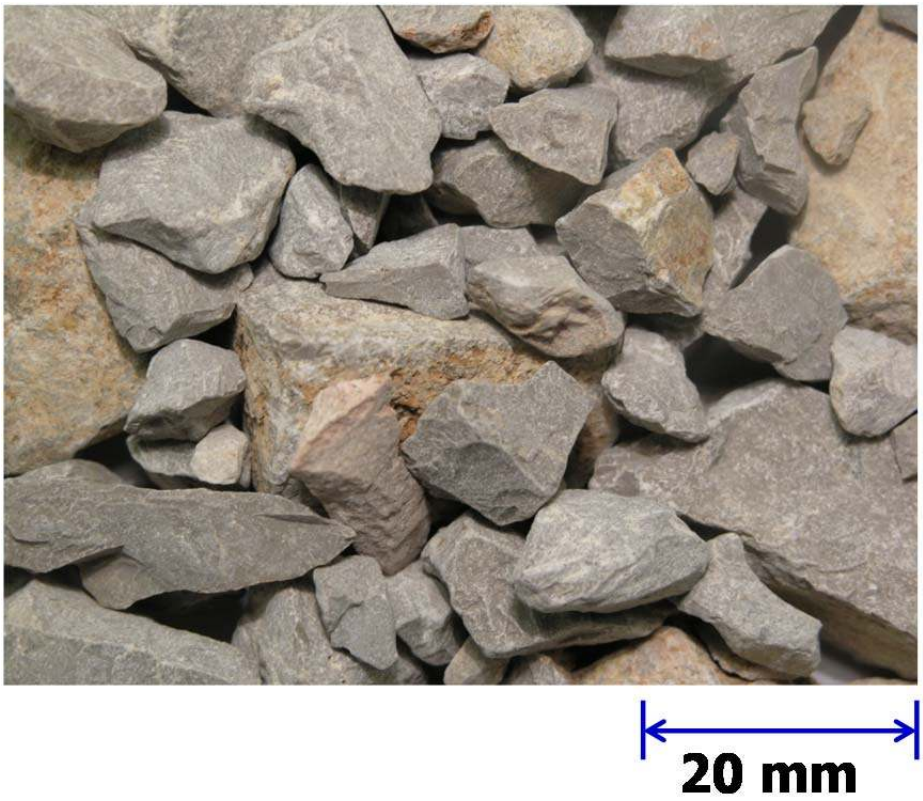

Figure 1: a) Pancrudo slate. b) Garraf limestone gravel.

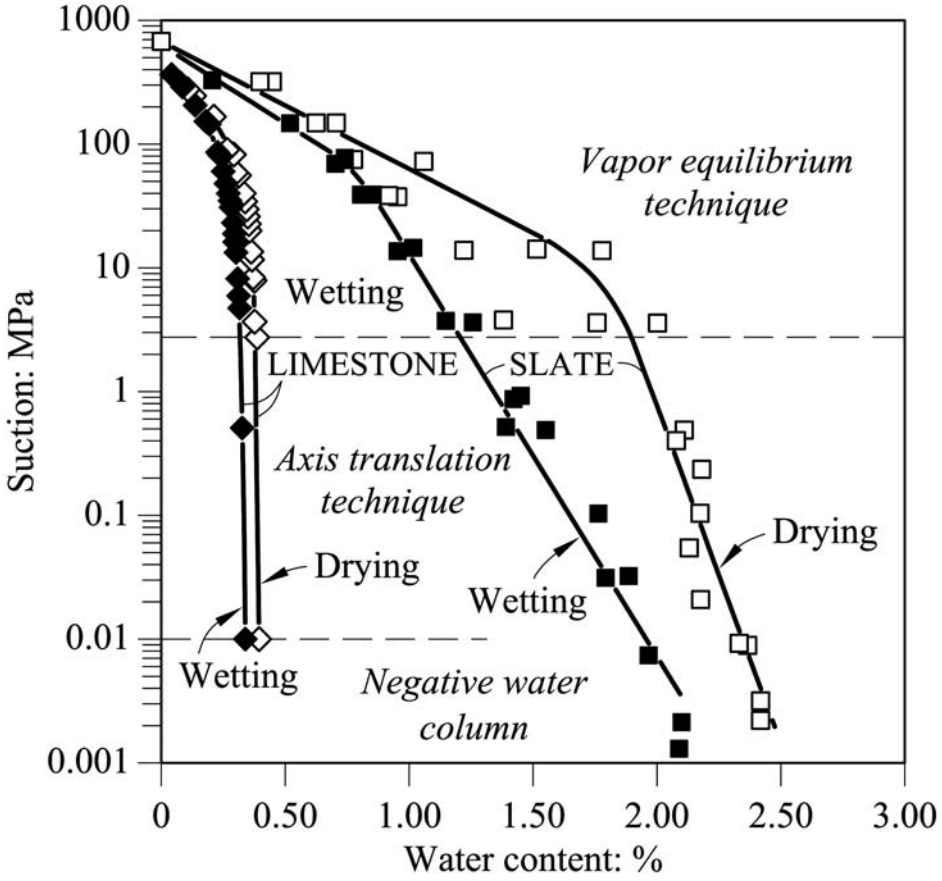

Figure 2: Limestone and slate retention curves.

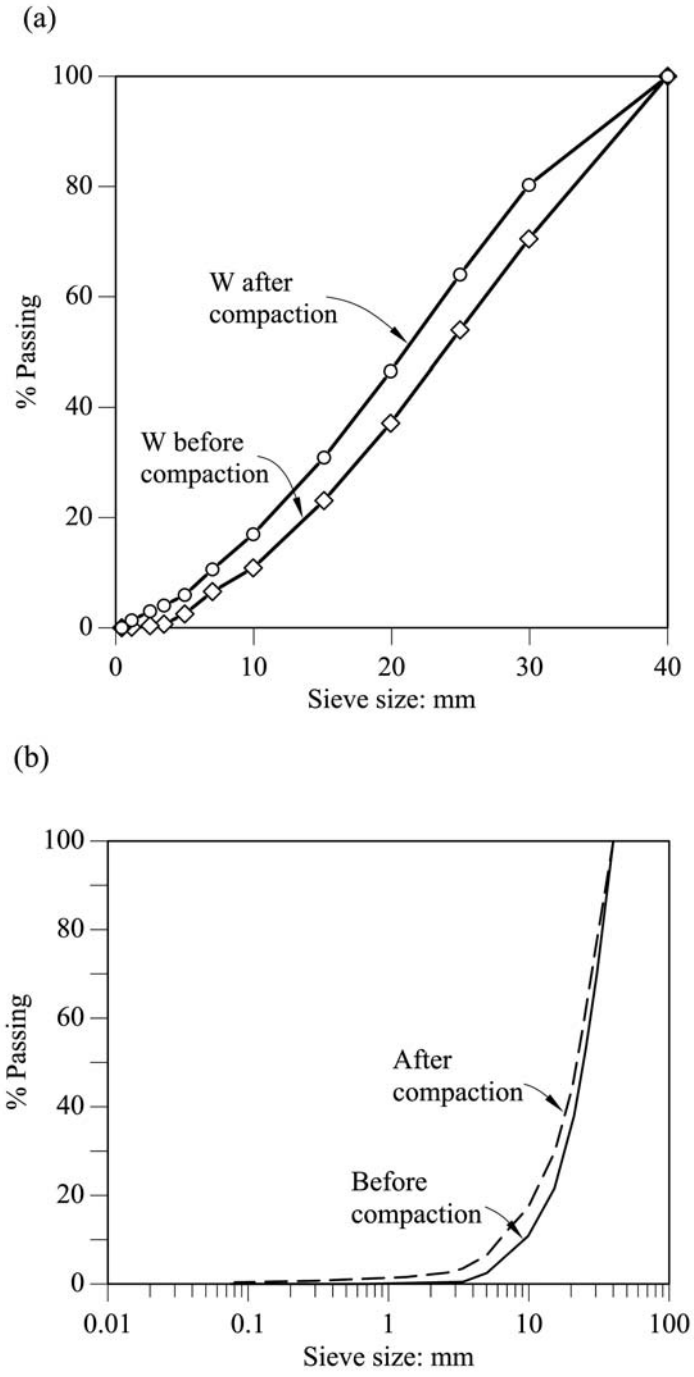

Figure 3: a) Grain size distributions of limestone gravel. *W*: Well graded samples. b) Grain size distributions of *W* limestone gravel and slate gravel before and after compaction (log scale of grain sizes).

Figure 4: a) Triaxial sample after installation of sensors for volume change; b) Placement of inner cell wall; c) Installation of outer cell wall.

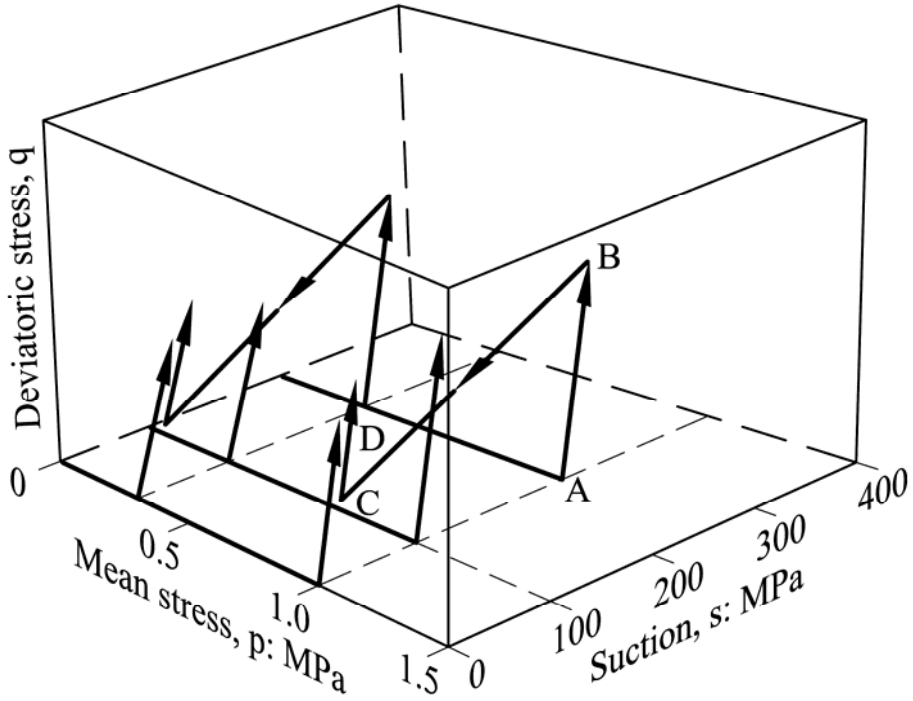

Figure 5: Stress paths on *W* limestone gravel samples plotted in a triaxial space (p, q, s).

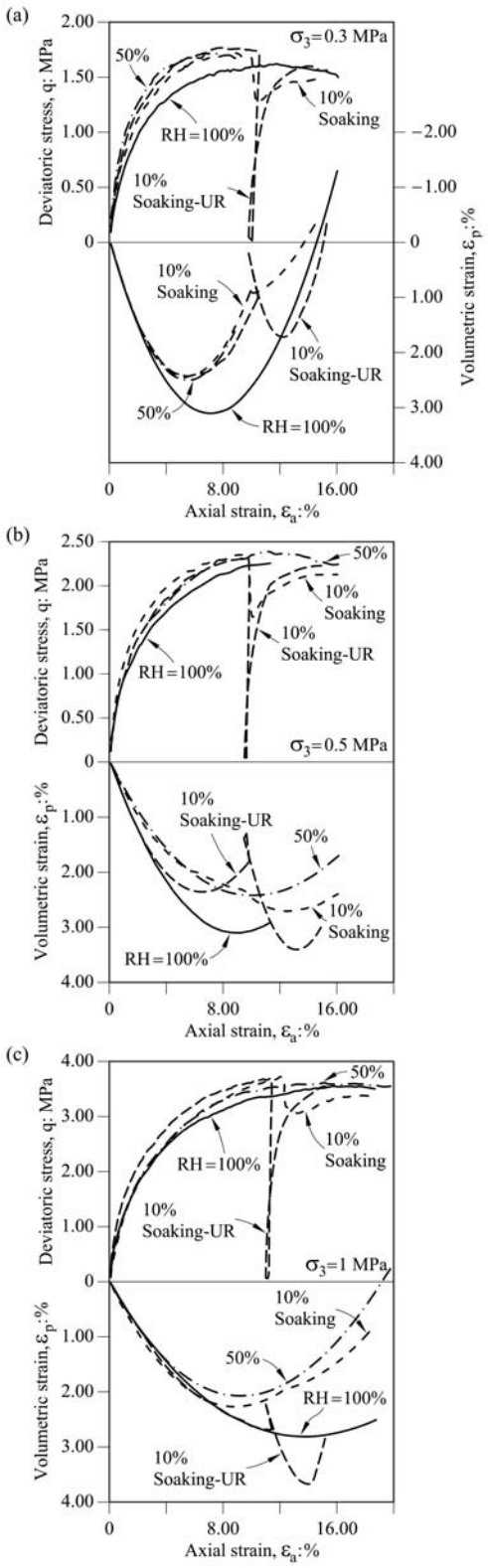

Figure 6: Suction controlled triaxial tests on *W* samples of Garraf limestone under a) σ_3 = 0.3 MPa; b) σ_3 = 0.5 MPa; c) σ_3 = 1 MPa.

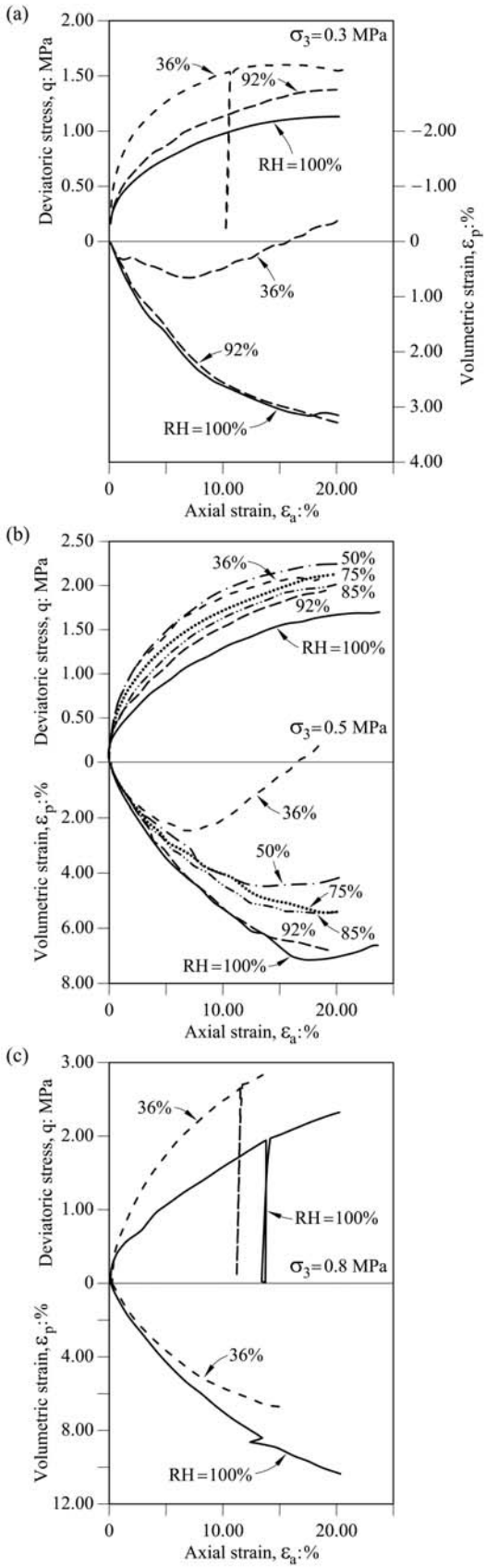

Figure 7: Suction controlled triaxial tests on Pancrudo slate under a) σ_3 = 0.3 MPa; b) σ_3 = 0.5 MPa; c) σ_3 = 0.8 MPa.

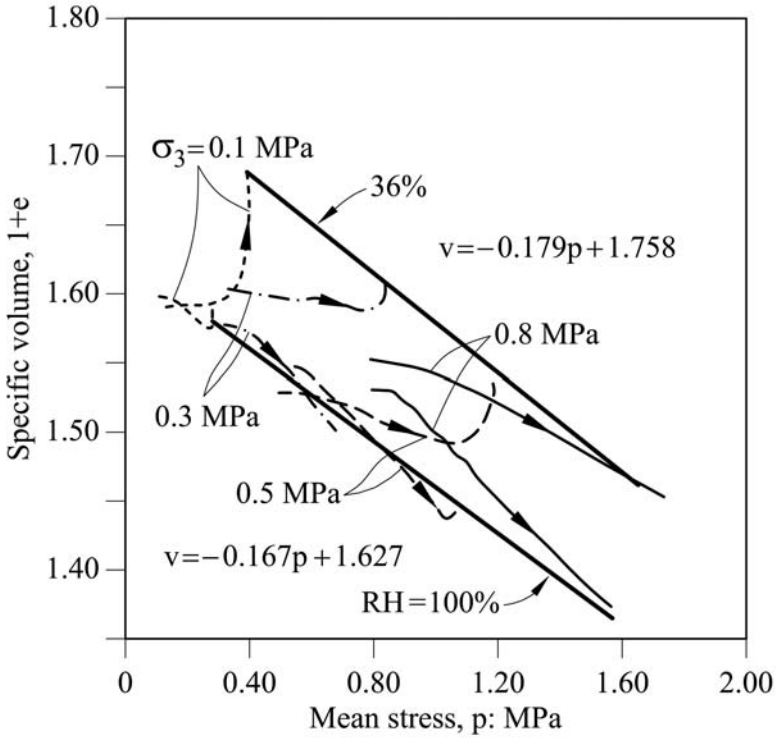

Figure 8: End of testing conditions, close to critical state, for Pancrudo slate.

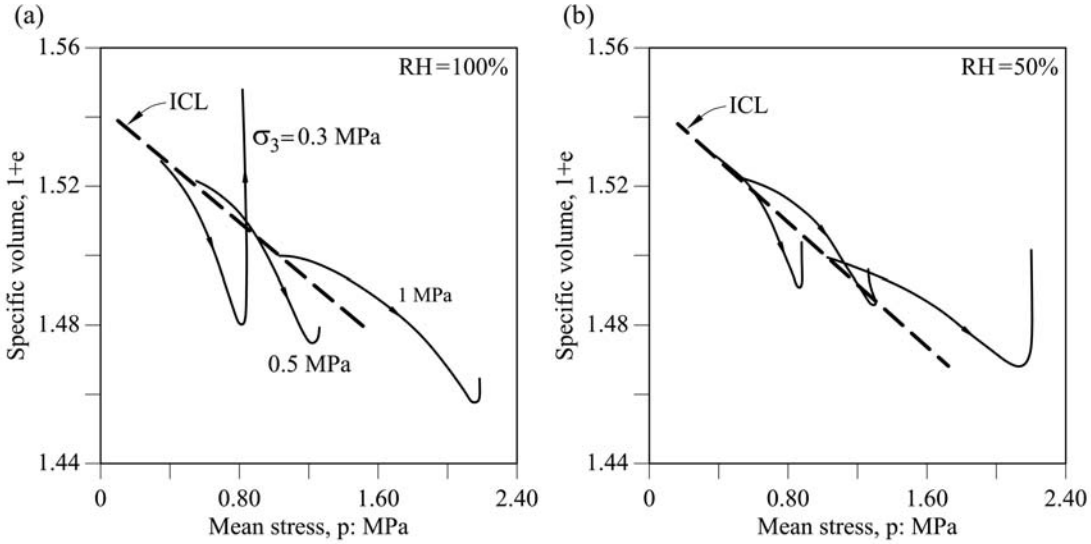

Figure 9: End of testing conditions for limestone gravel. a) *RH* = 100%; b) *RH* = 50%.

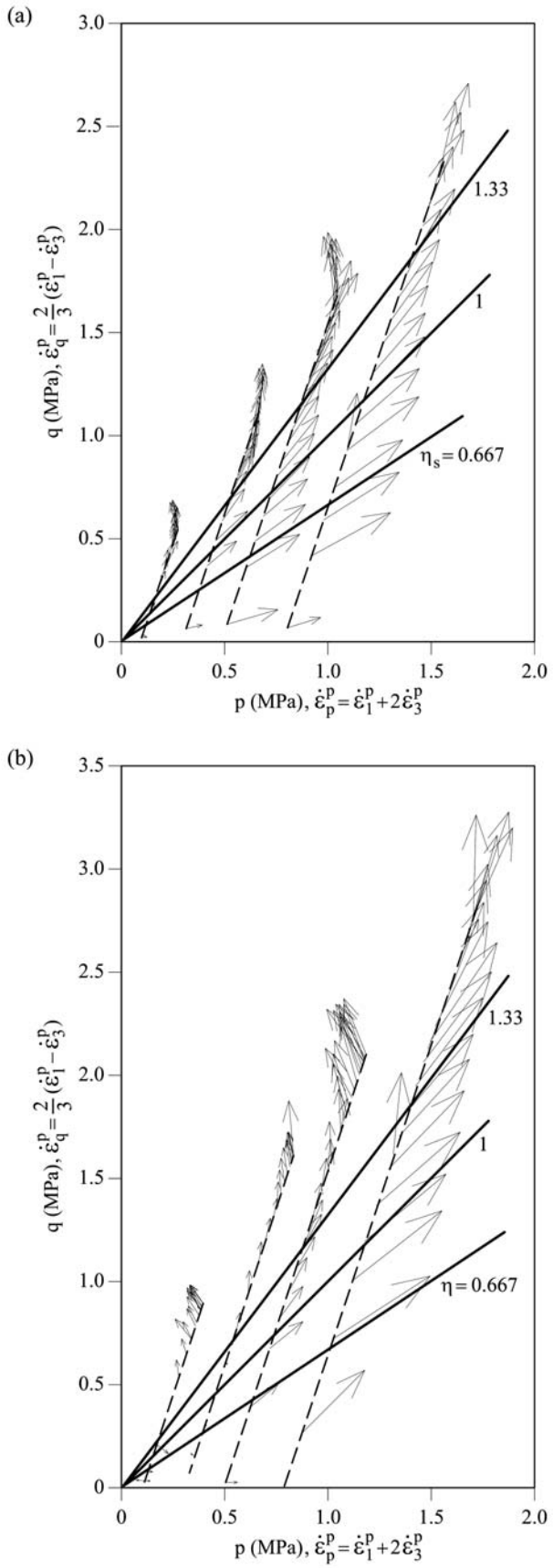

Figure 10: Plastic increment vectors. Triaxial tests on Pancrudo slate. a) *RH* = 100%; b) *RH* = 38%.

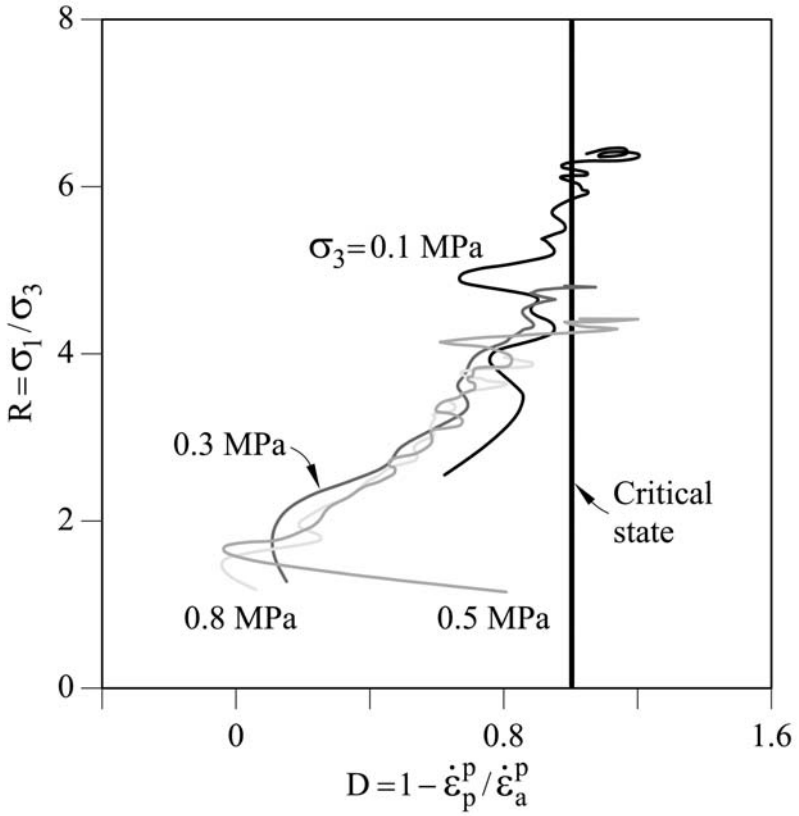

Figure 11: Dilatancy in triaxial tests of saturated samples of Pancrudo slate.

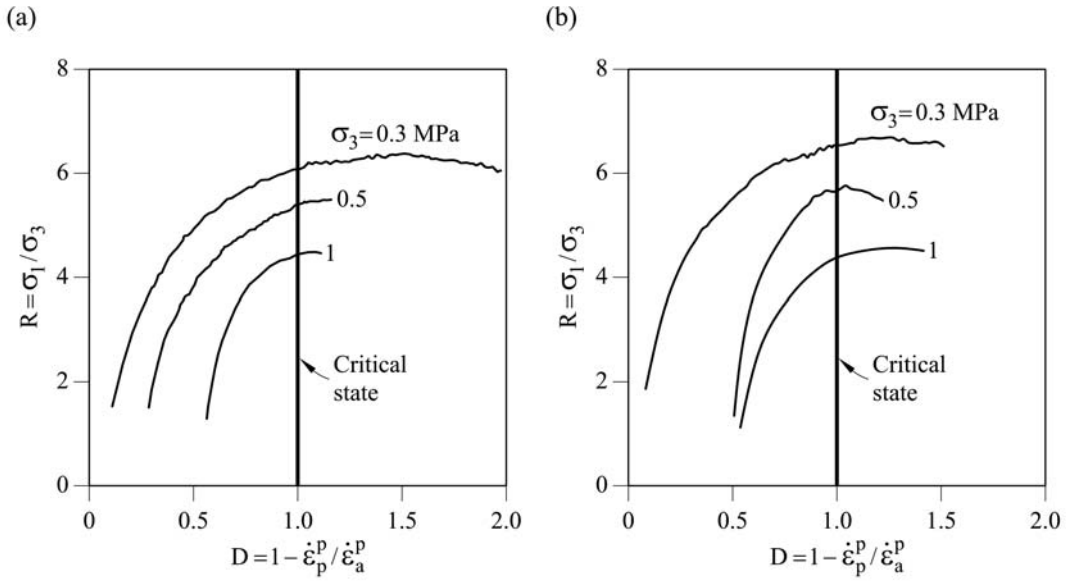

Figure 12: Dilatancy in triaxial tests samples of Garraf limestone. a) *RH* = 100%; b) *RH* = 50%.

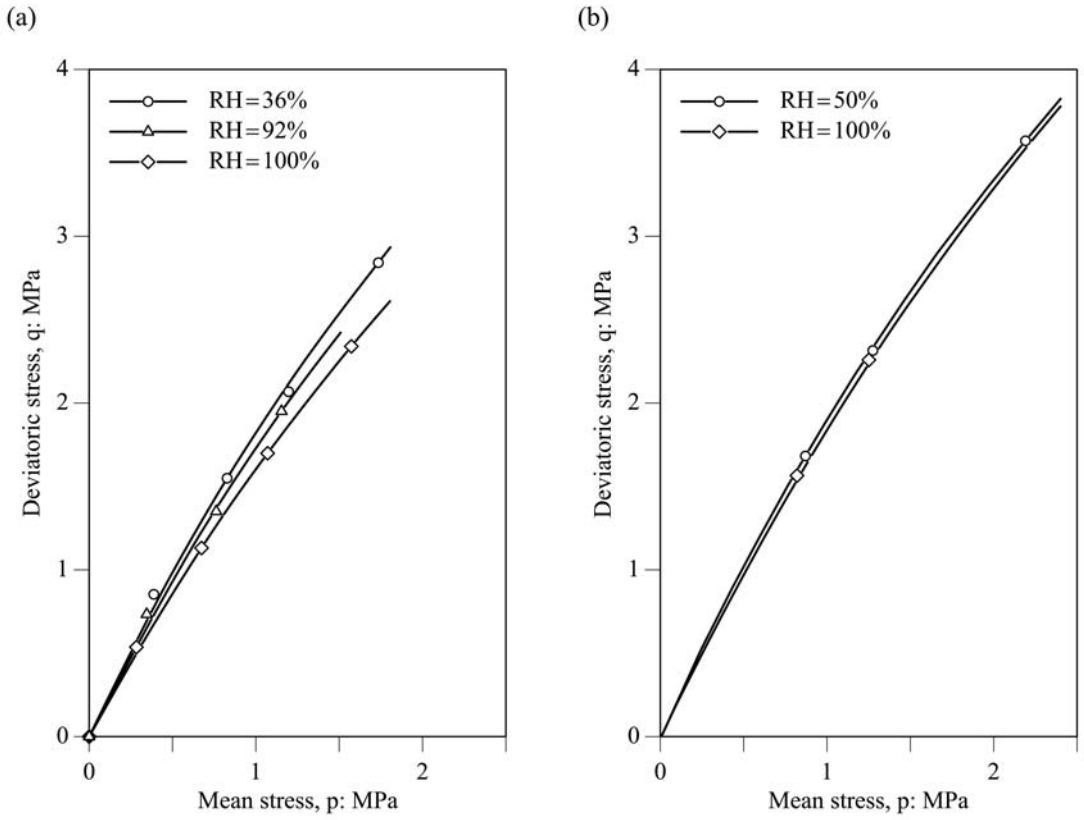

Figure 13: Strength envelopes. a) Pancrudo slate; b) Garraf limestone.

(a)

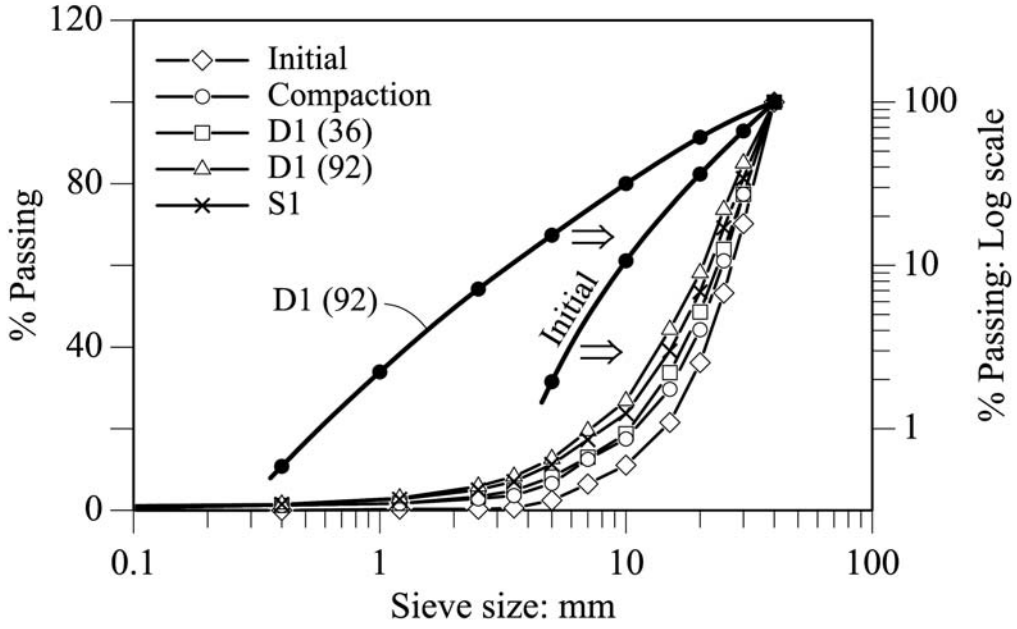
Initial
Compaction
D1 (36)
D1 (92)
S1
D1 (92)
Initial
% Passing
% Passing: Log scale
Sieve size: mm
120
80
40
0
100
10
1
0.1
1
10
100

(b)

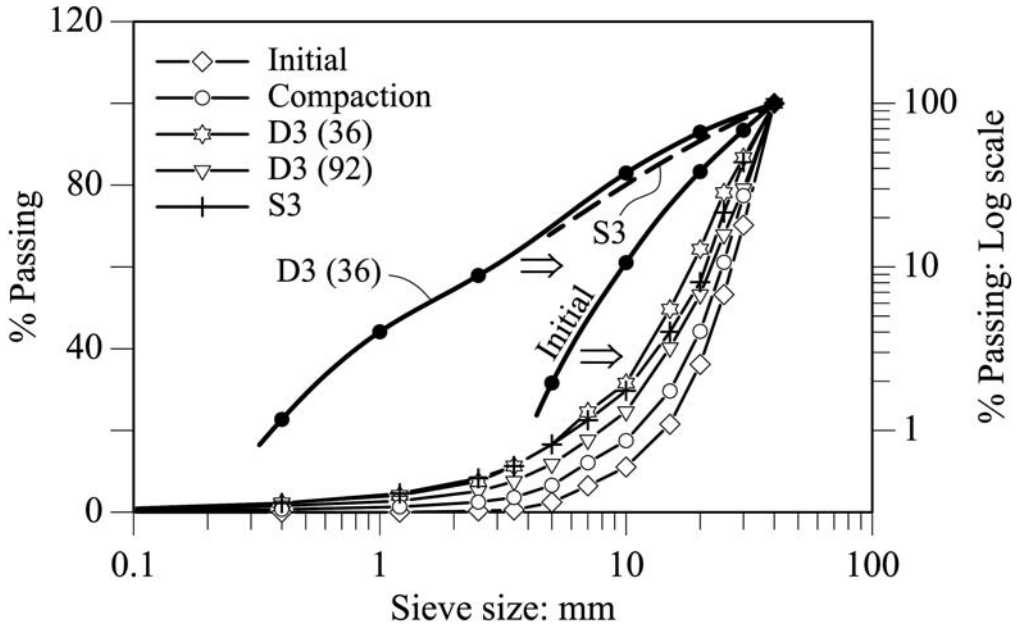
Initial
Compaction
D3 (36)
D3 (92)
S3
S3
D3 (36)
Initial
% Passing
% Passing: Log scale
Sieve size: mm
120
80
40
0
100
10
1
0.1
1
10
100

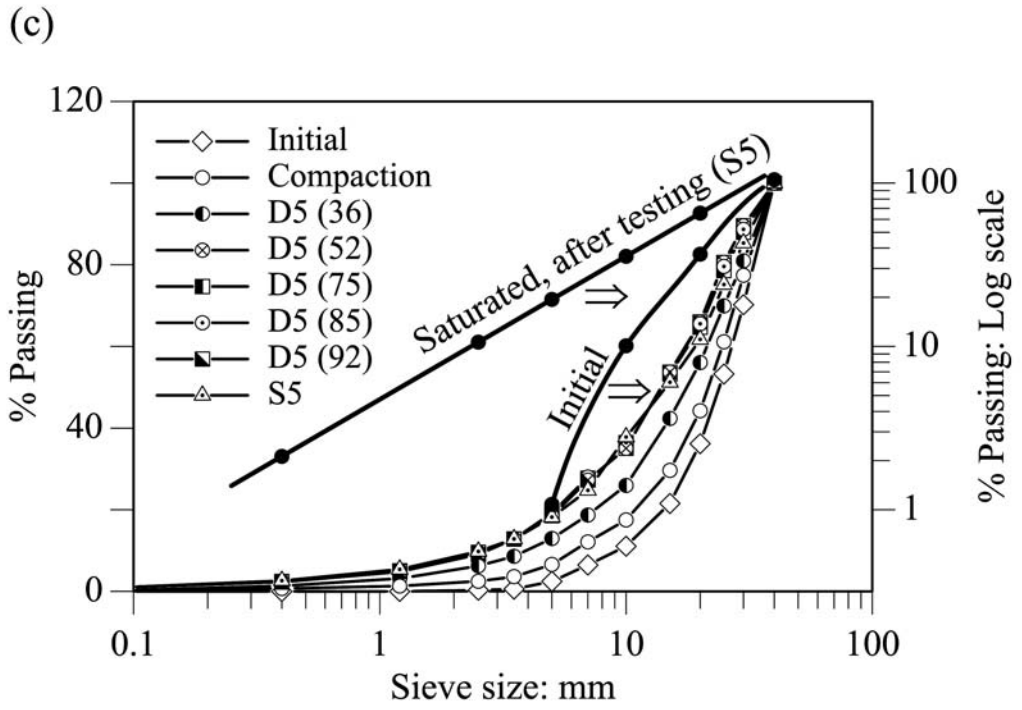

Figure 14: Evolution of grain size distribution of Pancrudo slate samples subjected to suction-controlled triaxial testing. a) σ_3 = 0.1 MPa; b) σ_3 = 0.3 MPa; c) σ_3 = 0.5 MPa. Numbers in parenthesis indicate the RH applied during testing. S identifies saturated conditions.

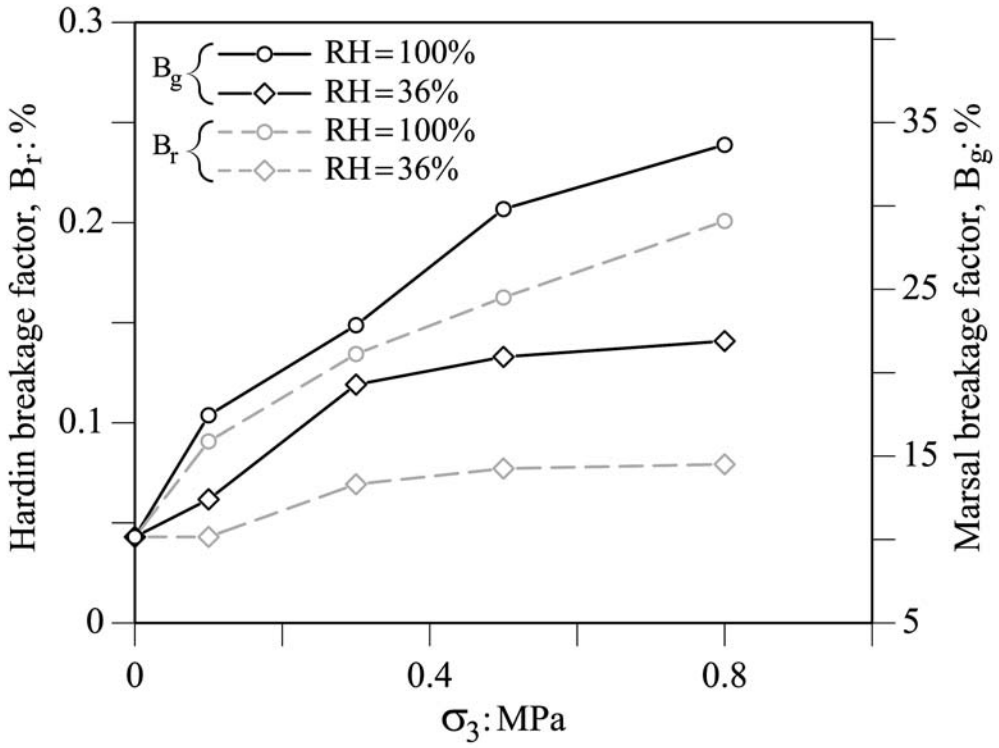

Figure 15: Evolution of breakage indices of slate samples subjected to suction-controlled triaxial testing.

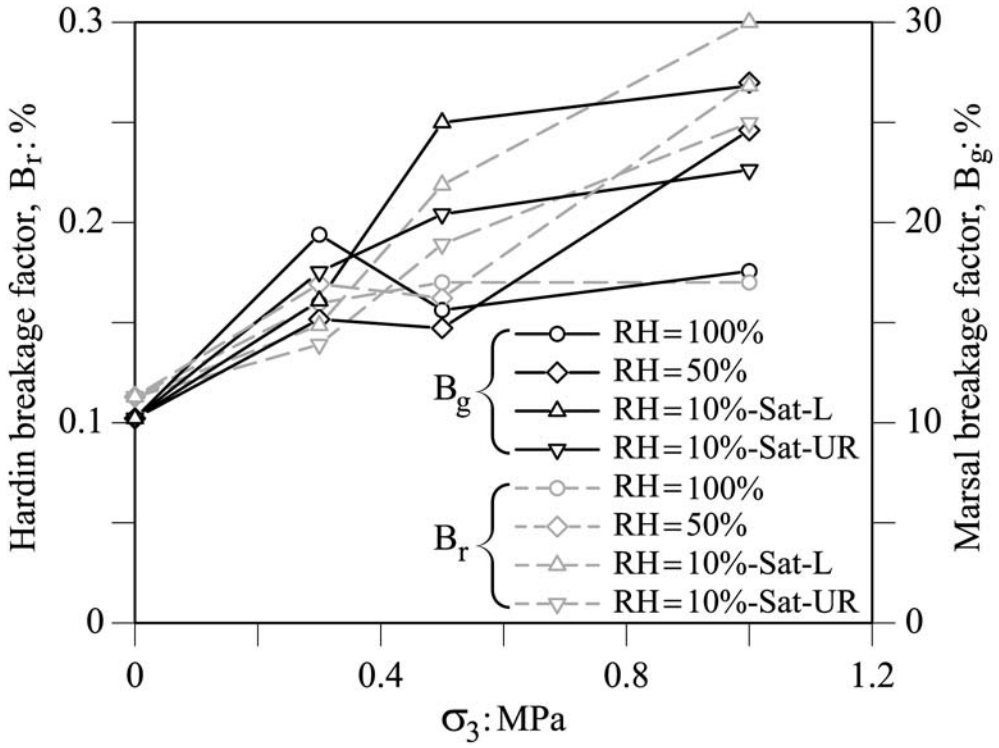

Fig. 16: Variation of Hardin and Marsal breakage indices for the applied stress and suction paths applied in terms of the confining stress. Suction controlled triaxial tests on Garraf limestone.

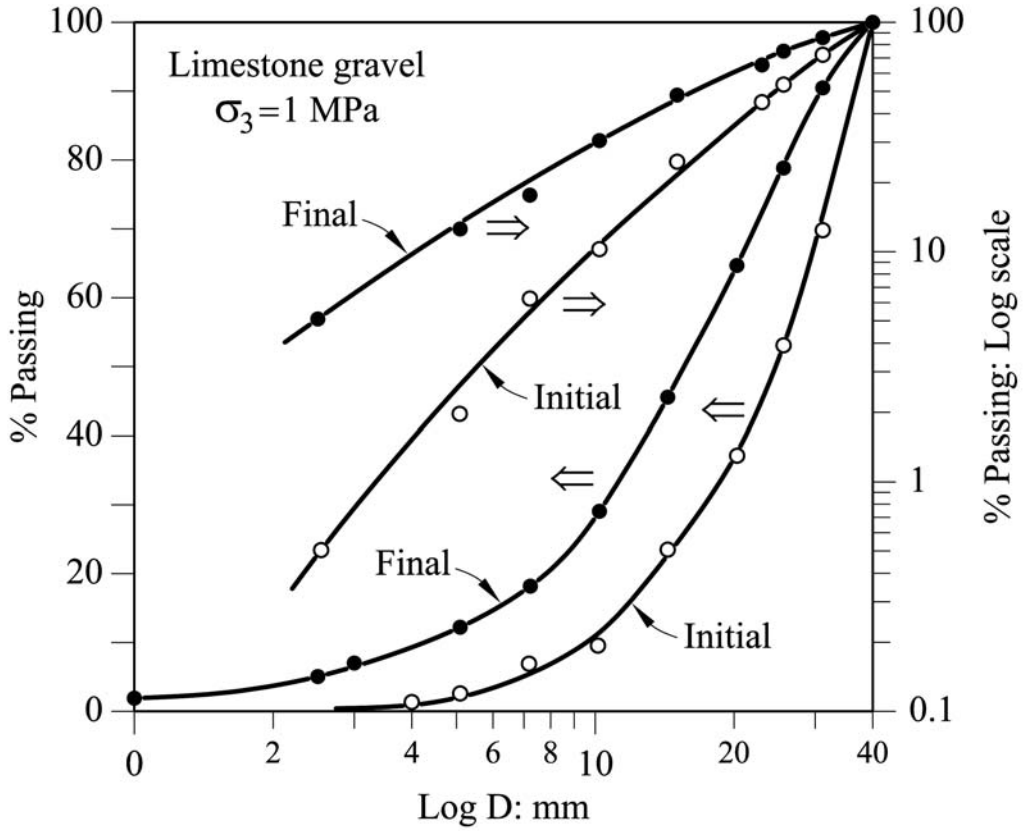

Figure 17: Evolution of grain size distribution of a limestone well graded sample subjected to suction-controlled triaxial testing at σ_3 = 1 MPa, wetted during straining, unloaded and reloaded.

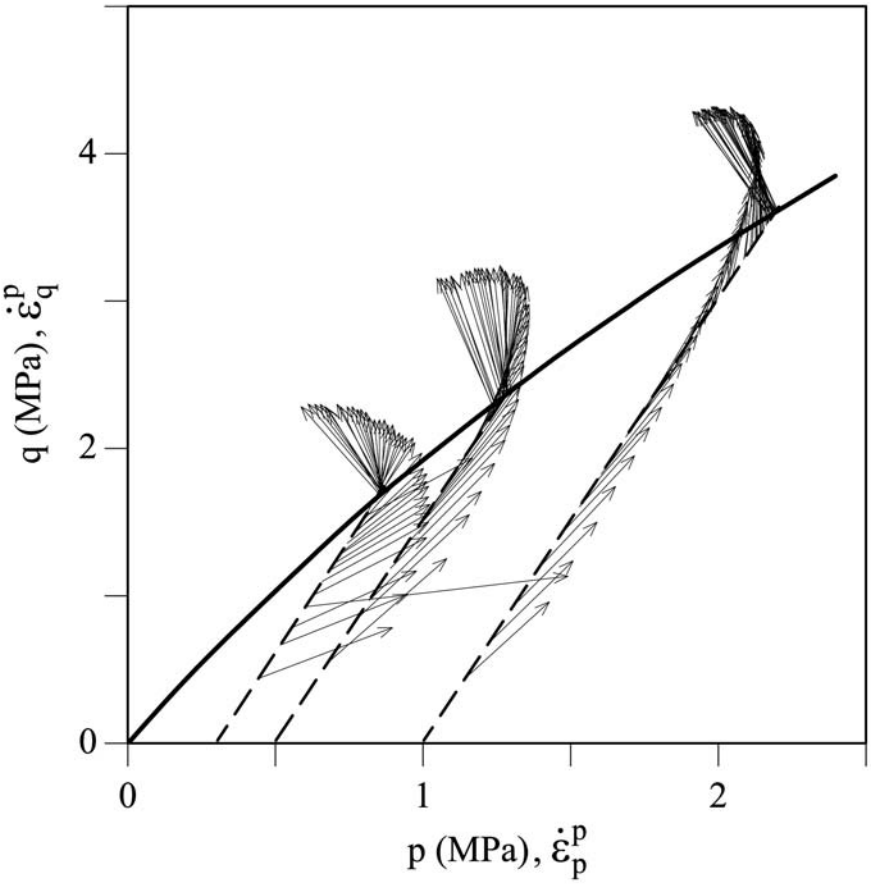

Figure 18: Plastic strain vectors along loading paths on limestone gravel at $RH = 50\%$.

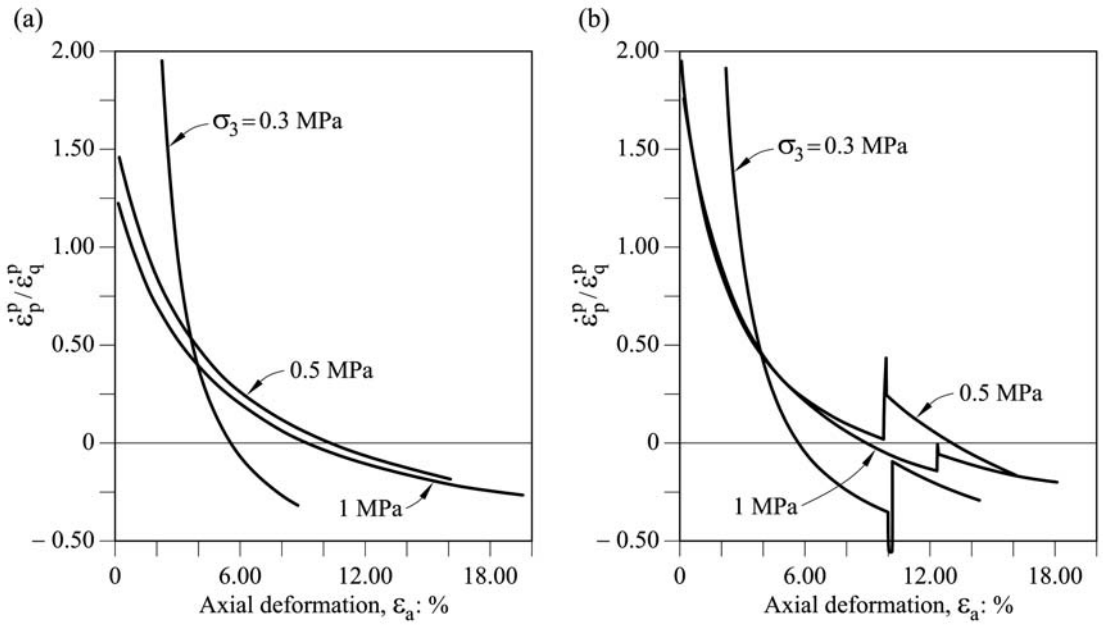

Figure 19: Dilatancy rate of tests on limestone gravel in terms of axial deformation and confining stress for a) *RH* = 50%; b) *RH* = 10% and soaking at an advanced state of shearing.

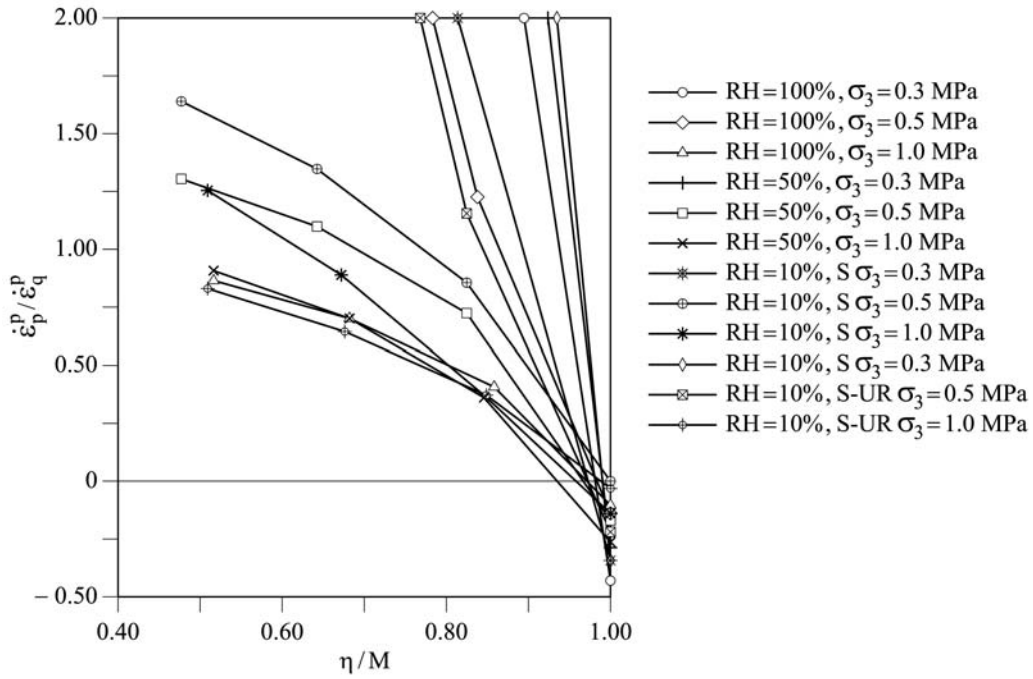

Figure 20: Dilatancy rate in terms of the normalized stress ratio, for the set of triaxial tests performed on limestone gravel. S: saturation; UR: Unloading-reloading.

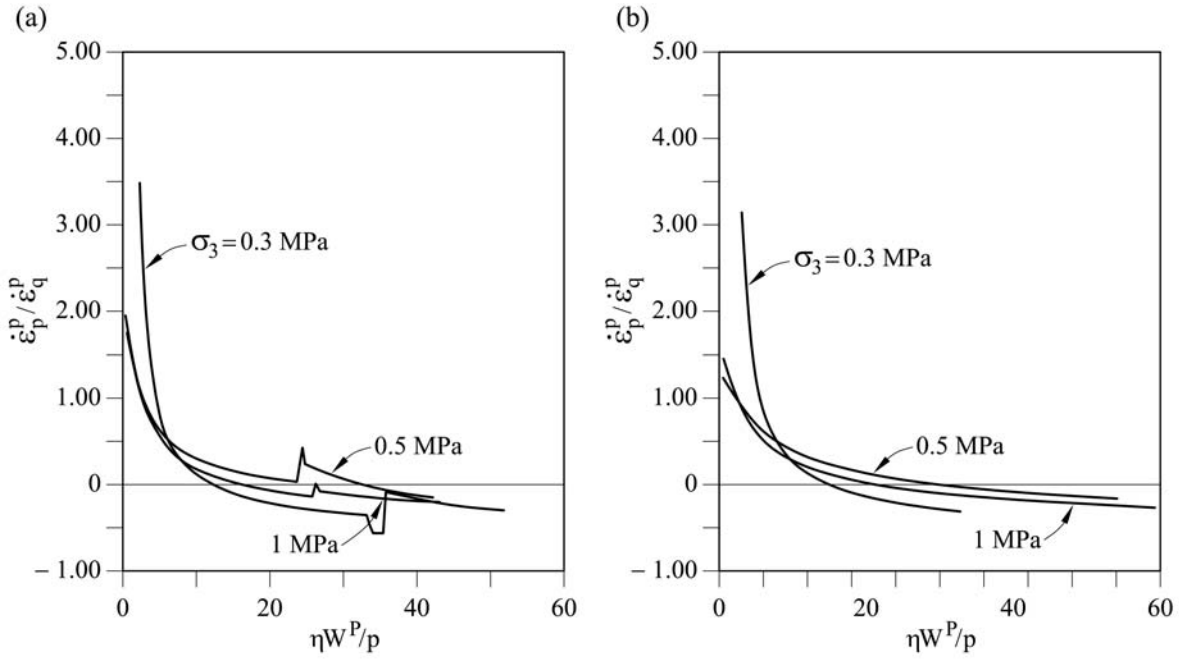

Figure 21: Dilatancy rate in terms of stress ratio and normalized plastic work, for the set of triaxial tests performed on limestone gravel. a) *RH* = 10% and saturated at advanced straining and b) *RH* = 50%.

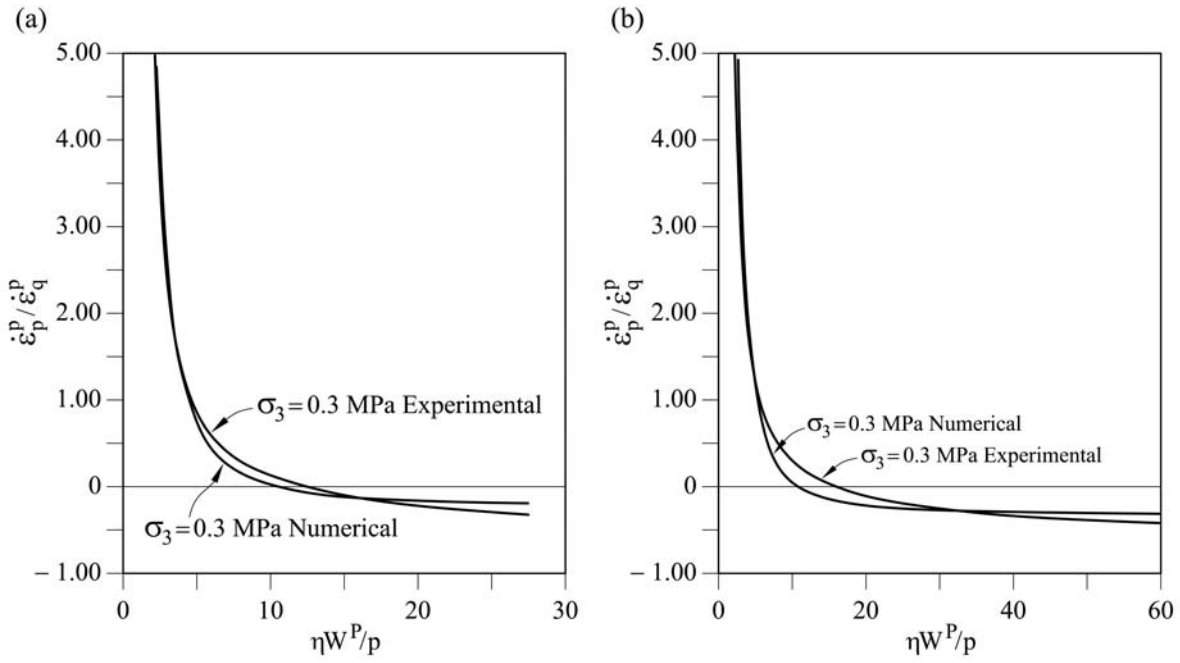

Figure 22: Comparison of measured and calculated (Eq. 9) dilatancy rates of hard limestone. a) *RH* = 50% and b) *RH* = 100%.

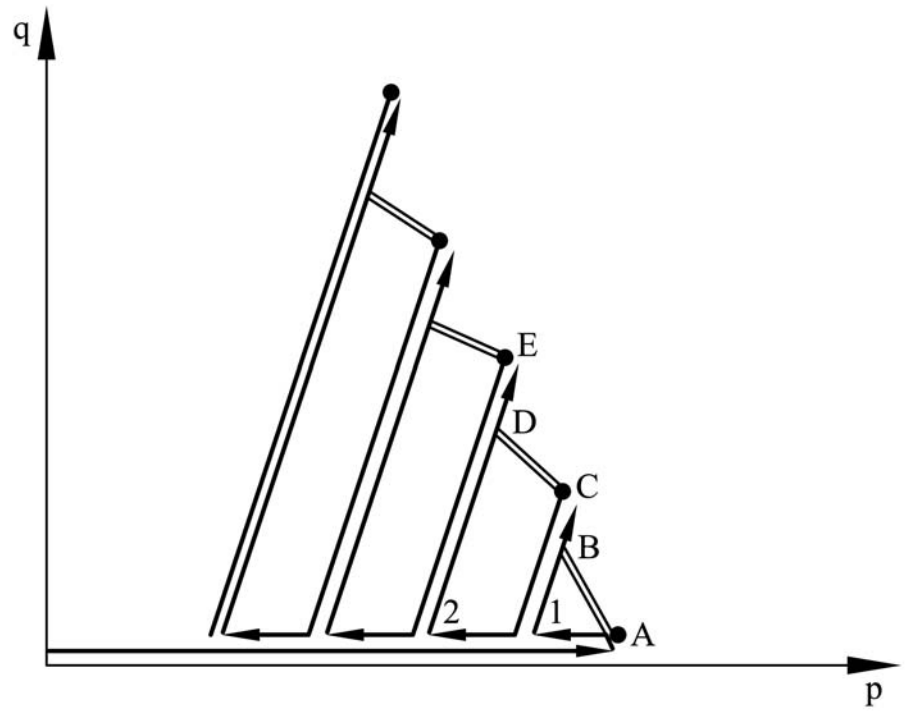

Figure 23: Stress paths to investigate the shape of the yield surface.

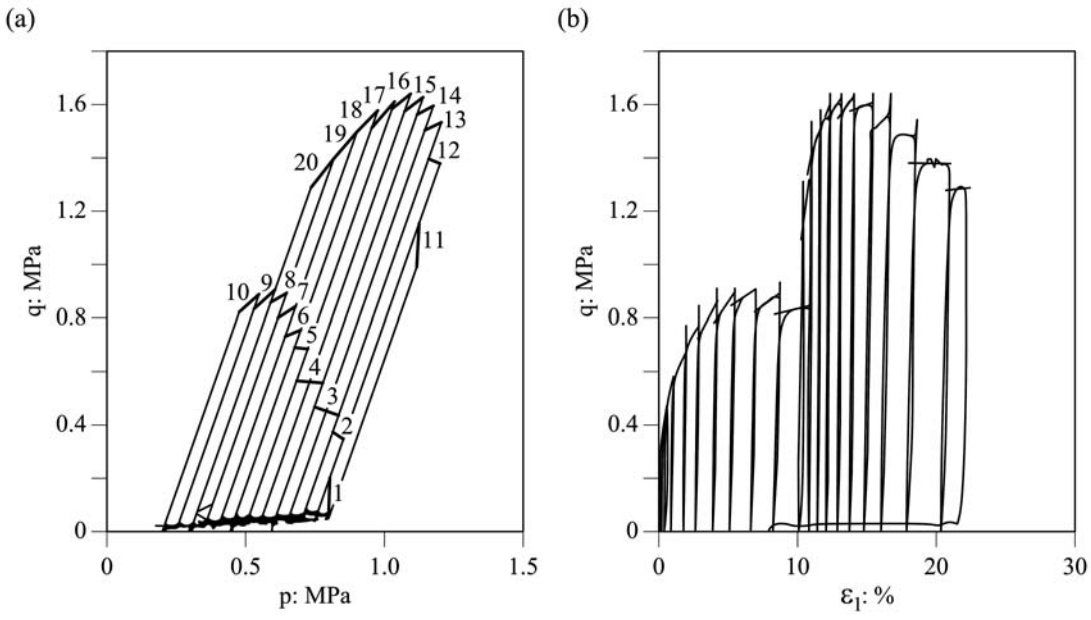

Figure 24: a) Imposed stress paths on a sample of compacted Pancrudo slate. b) Measured response.

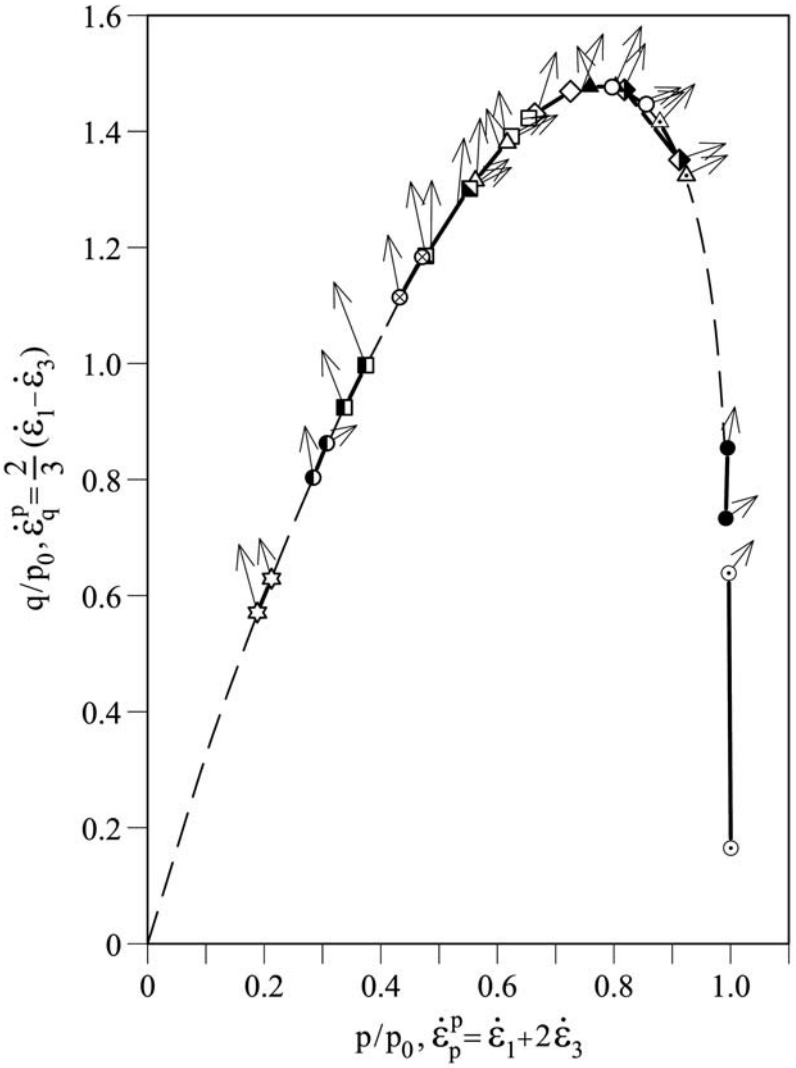

Figure 25: Yield surface and plastic strain increment for triaxial conditions. Saturated compacted Pancrudo slate.

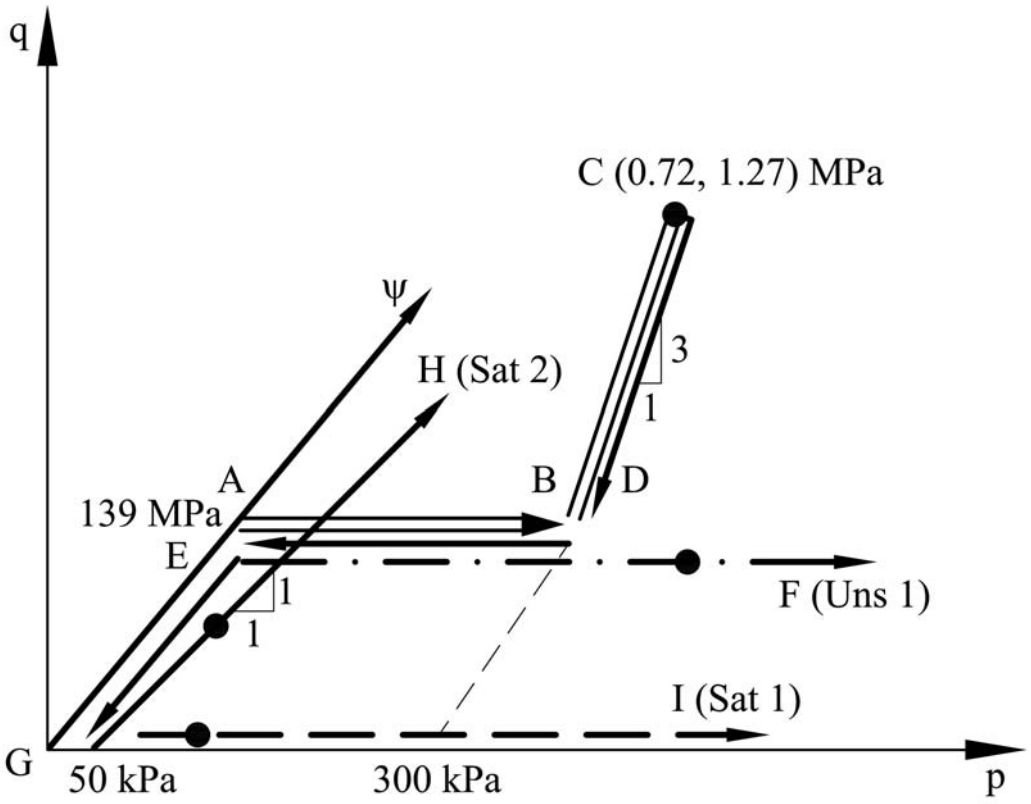

Figure 26: Stress paths for a wetting path after equilibration at a total suction of 139 MPa. Slate gravel.

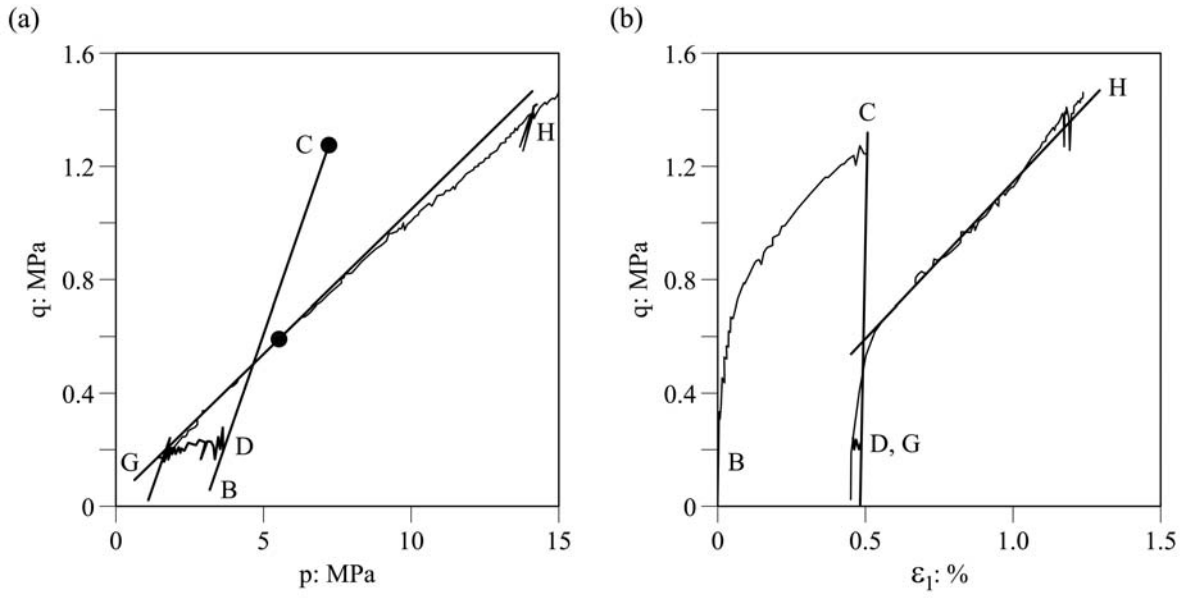

Figure 27: a) Stress path applied in test Sat2 on slate gravel; also indicated are the yielding points. b) Sample response.

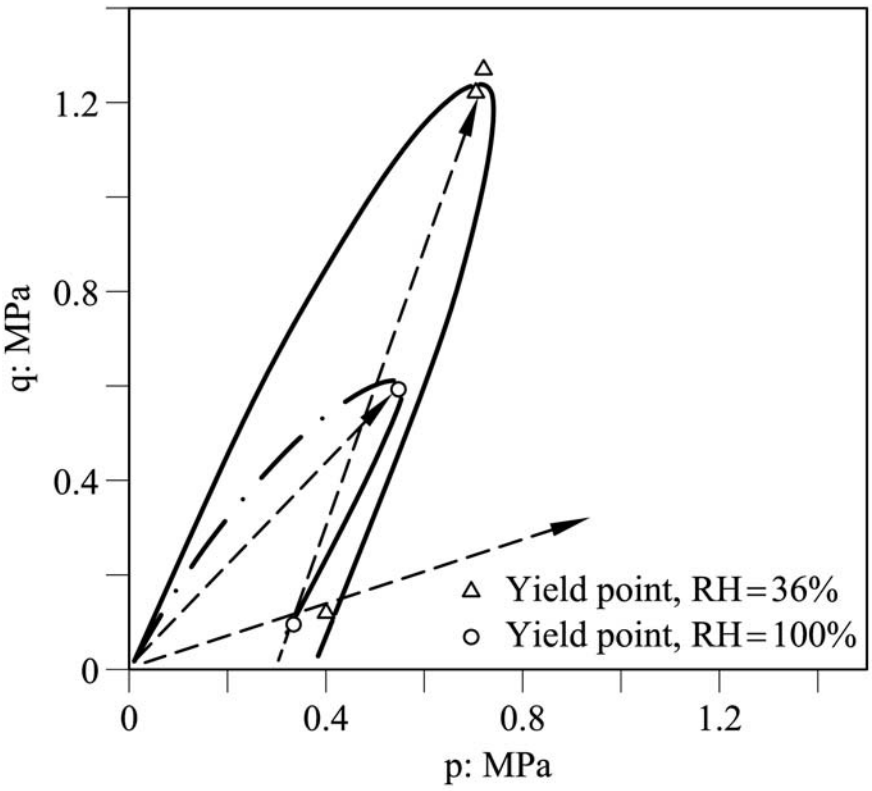

Figure 28: Yielding points and yielding locus for two value of Relative Humidity. Compacted slate gravel.

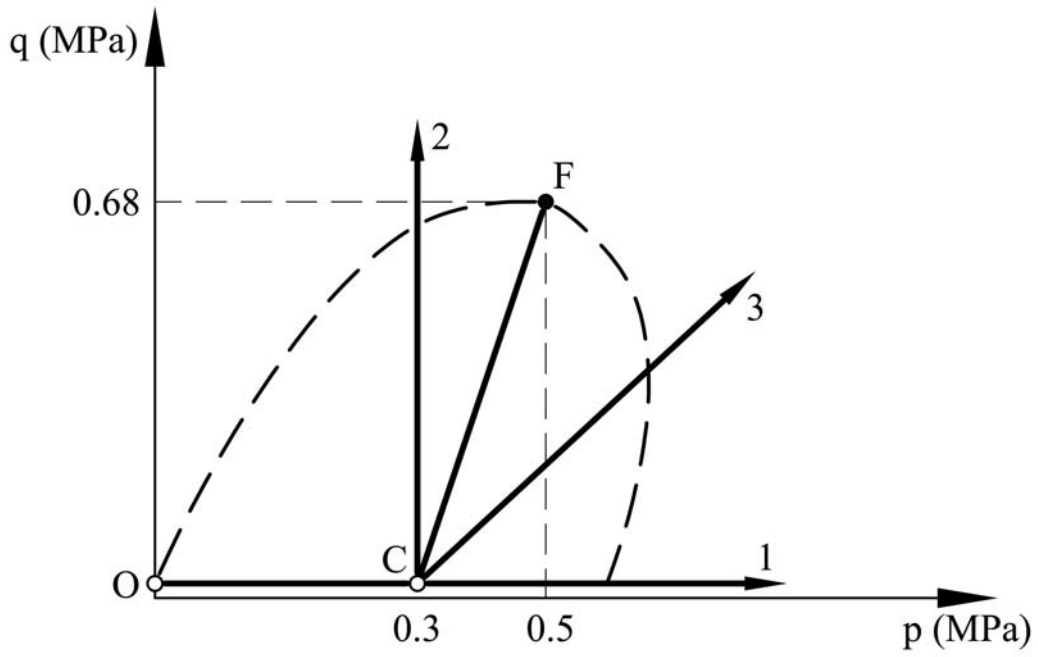

Figure 29: Stress paths for the determination of the shape of the yield surface under varying suction.

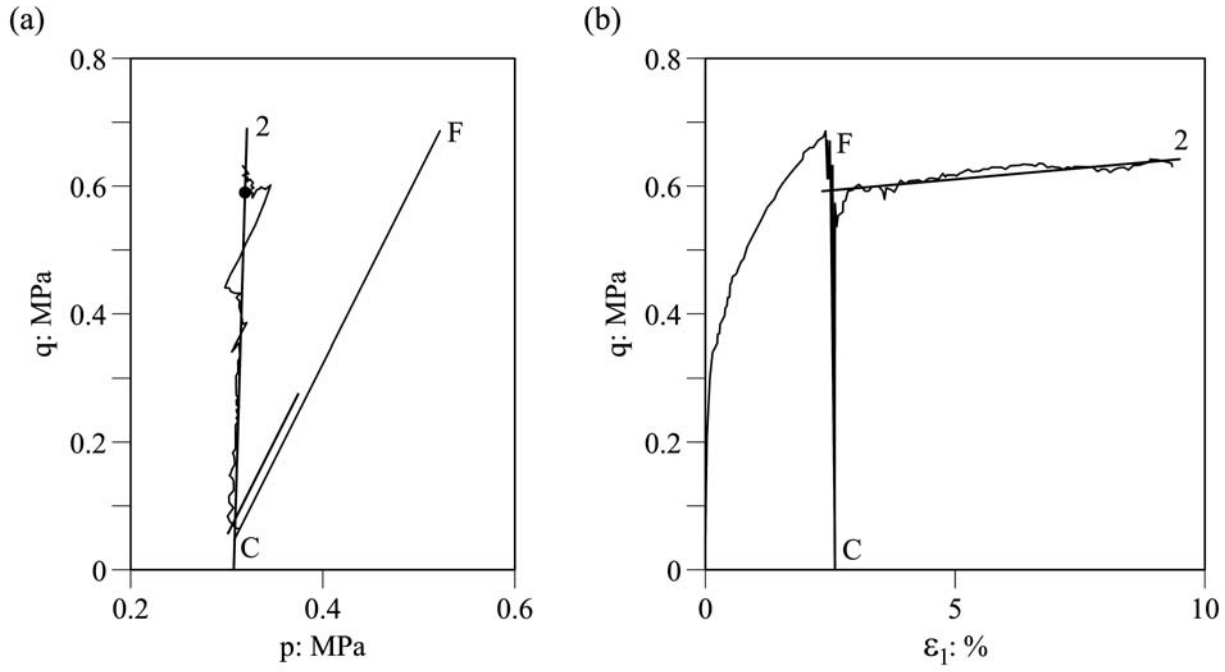

Figure 30: a) Stress path for unloading (FC) and loading along C2. B) Sample response. Test on saturated compacted Pancrudo slate. Yielding point along C2 is marked in a).

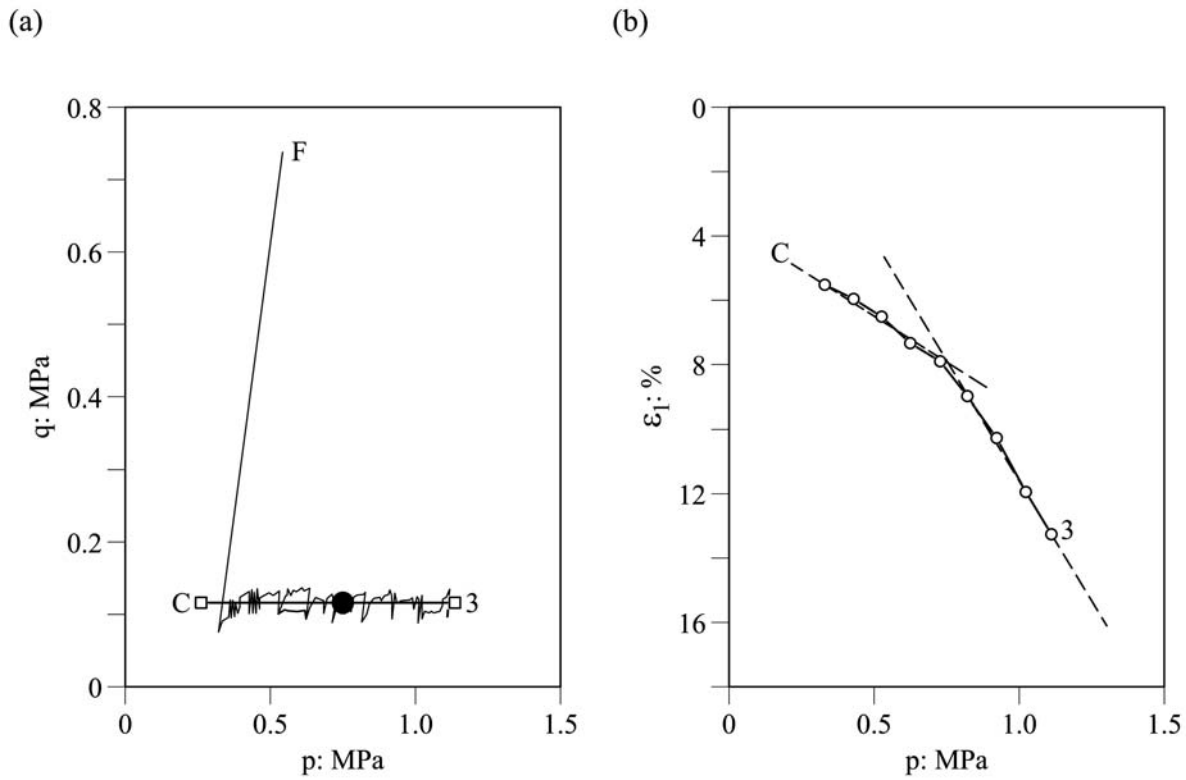

Figure 31: a) Stress path for unloading (FC) and loading along C3. b) Sample response. Test on unsaturated (RH = 42%) compacted Pancrudo slate. Yield point along C3 is marked in a).

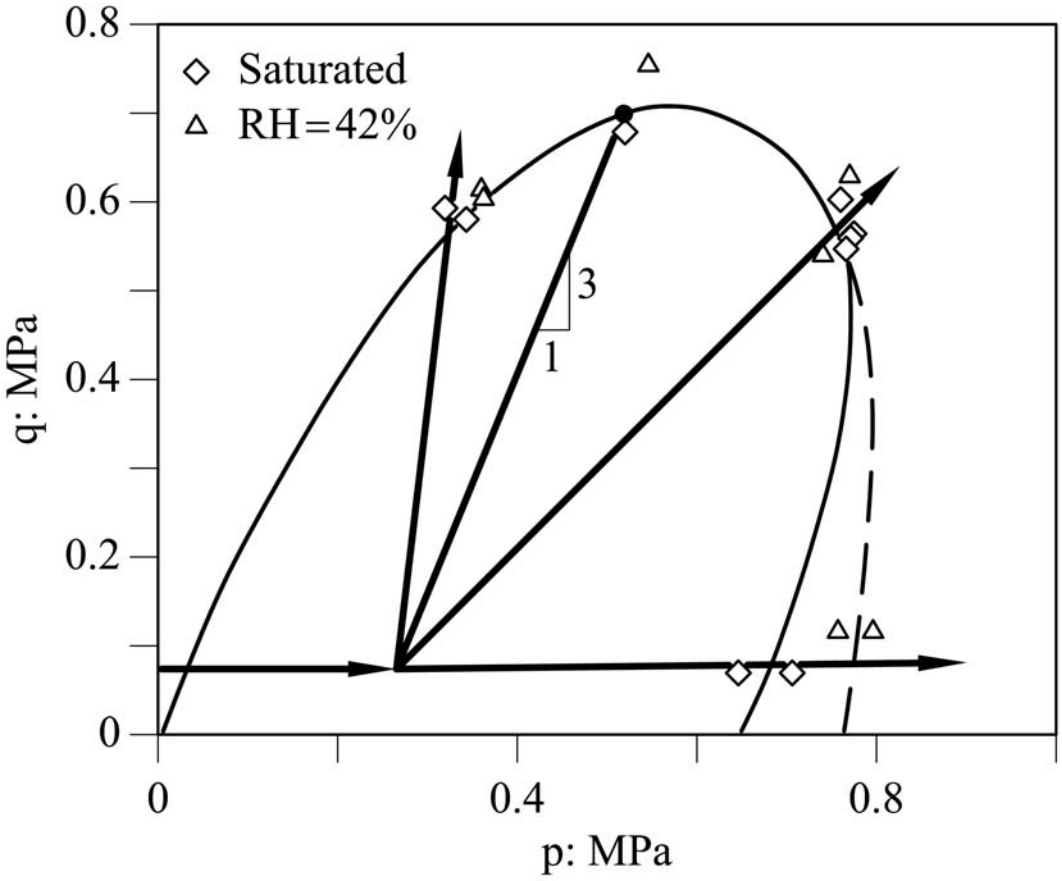

Figure 32: Yielding points and estimated yield surfaces for compacted samples of Pancrudo slate gravel equilibrated initially to identical stress state. Tests for saturated and unsaturated states (RH = 42%) are represented in the same plot.

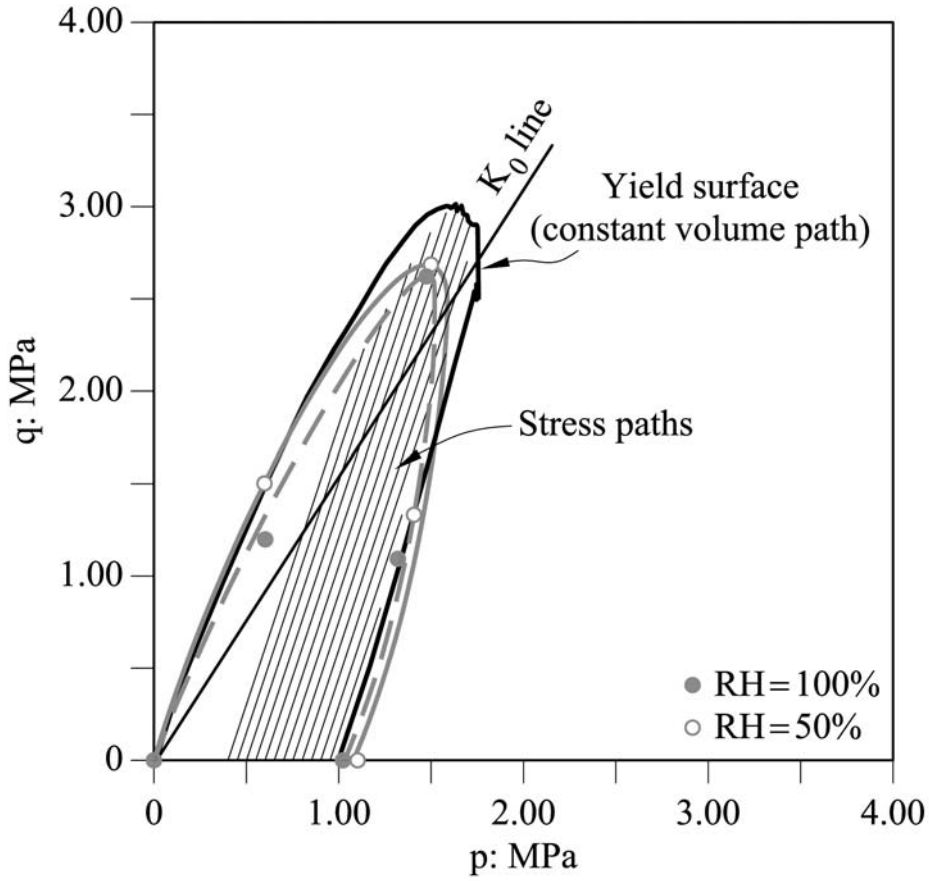

Figure 33: Yield surface of compacted limestone gravel at a relative humidity *RH* = 50%. Outer locus determined in constant volume stress path in a sample initially confined to *p* = 1 MPa. Elastic linear paths obtained by loading the sample in stages at decreasing confining stress once the sample was initially compressed to *p* = 1 MPa. Also shown is the yielding domain obtained in radial stress paths shown in Figure 36 for two Relative Humidities (50% and 100%).

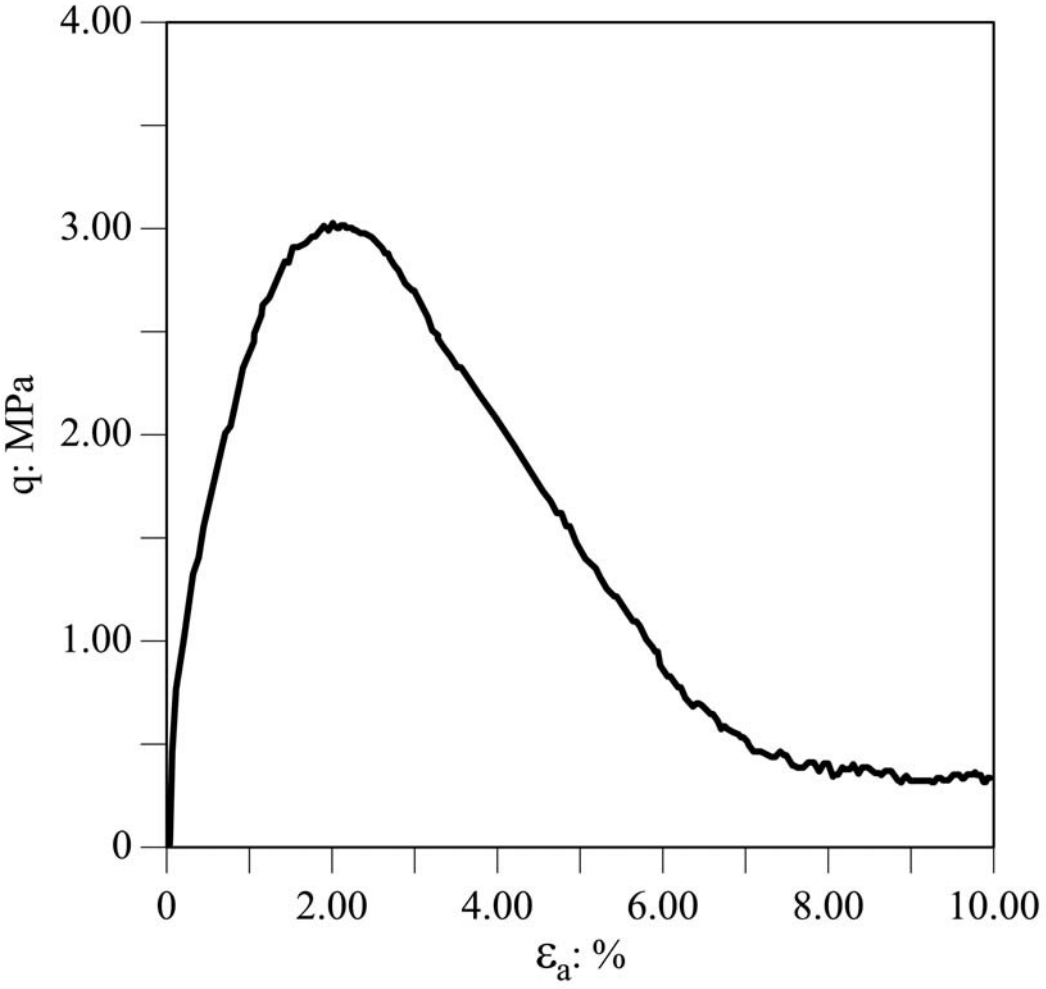

Figure 34: Recorded deviatoric stress in a constant volume test of a limestone sample at a $RH = 50\%$.

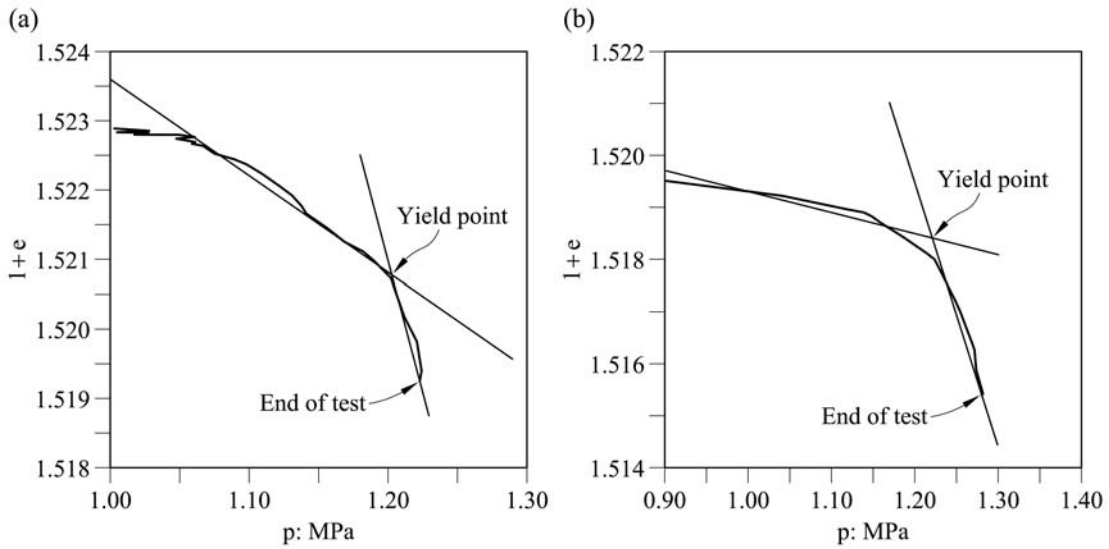

Figure 35: Yielding points during multistage loading at decreasing confining stress on limestone gravel at $RH = 50\%$.

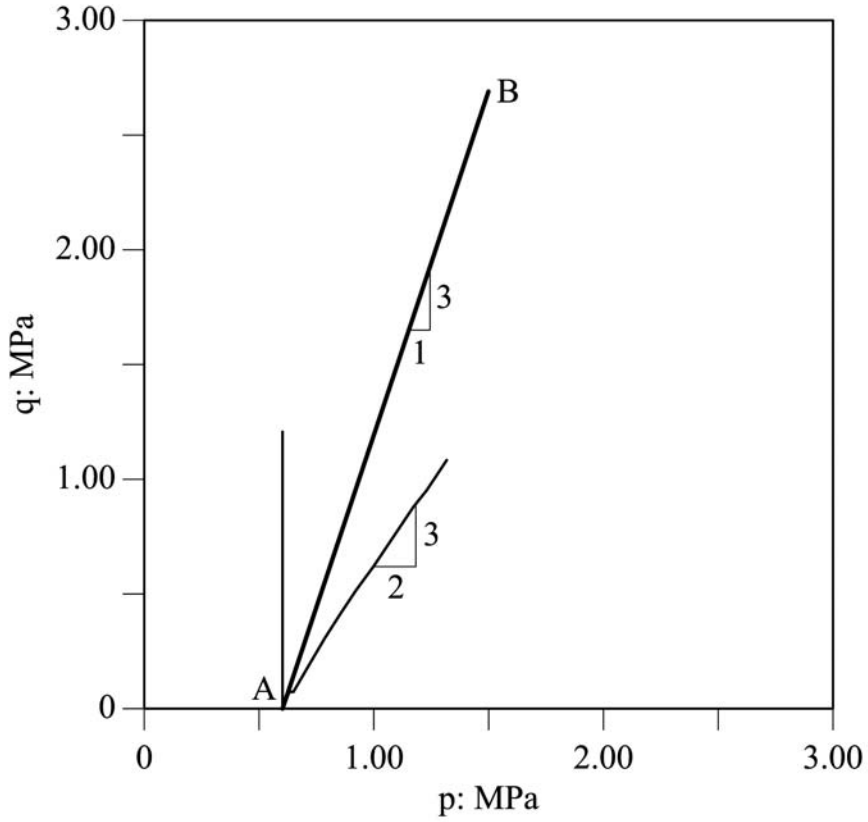

Figure 36: Applied stress paths to limestone samples. Two test series were performed: at $RH = 100\%$ and $RH = 50\%$.

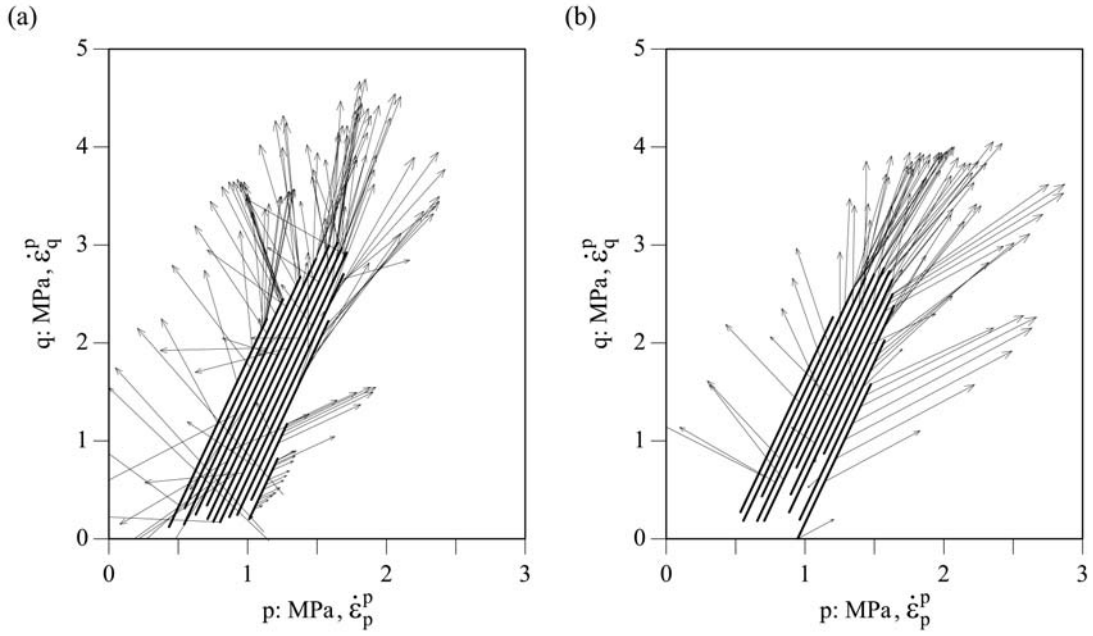

Figure 37: Incremental plastic strain vectors measured in multistage tests on compacted limestone gravels. a) *RH* = 50%; b) *RH* = 100%.